



Hindered Transport of Bacteria in Porous Media Flows

Submitted by
Amin Dehkharghani

in partial fulfillment of the requirements for the degree of
Master's of Science
in
Mechanical Engineering

School of Engineering
Tufts University
Medford, Massachusetts

May 2017

Certified By:

Jeffrey S. Guasto
Department of Mechanical Engineering
Tufts University

Committee:

Marc Hodes
Department of Mechanical Engineering
Tufts University

Committee:

C. Andrew Ramsburg
Department of Civil and Environmental Engineering
Tufts University

Acknowledgements

I owe a debt of gratitude to my advisor Professor Jeffrey Guasto and his postdoctoral associate Dr. Nicolas Waisbord for their extraordinary support and guidance during my graduate education and research. I would like to acknowledge Professor Jörn Dunkel from MIT for his helpful insights and suggestions on this project. I would like to thank my thesis committee, Professors Marc Hodes and Andrew Ramsburg for their encouragement and detailed analysis of this work.

Abstract

Swimming bacteria play crucial roles in processes ranging from the biodegradation of pollutants in groundwater to the spread of infections in the human body. The environments inhabited by these motile cells are characterized by porous microstructure and dynamic fluid flows. We show that the complex interplay between motility, geometry, and flow can lead to heterogeneous distributions of bacteria and severely hindered bacterial transport properties. Using video microscopy, we track the motion of bacteria (*Bacillus subtilis*) flowing through a microfluidic porous medium and complement these measurements by Langevin simulations. Cell trajectories reveal filamentous patterns of high cell concentration that result from the orientational coupling of cell elongation to the flow (Jeffery orbits) and steric surface interactions. The effective diffusion coefficient of the bacteria is severely hindered in the transverse flow direction with increasing mean shear rate due to the faster decorrelation of the cells' orientation by shear.

Table of contents

List of figures	vi
1 Introduction	1
2 Microfluidic Experiments and Langevin Simulations	7
2.1 Model Microfluidic Porous Media and Swimming Bacteria	7
2.1.1 Microfluidic Device Design, Fabrication, and Characterization	7
2.1.2 Bacterial Cell Culturing	8
2.1.3 Microfluidic Assays and Analyses	9
2.2 Langevin Simulations of Bacterial Motility in Porous Media Flows	10
2.2.1 Modeling Run and Tumble Motion with Rotational Diffusion	11
2.2.2 Equations of Motion of Bacteria in 2D Stokes Flow	12
2.2.3 Numerical Simulation of Flow through 2D Porous Media	14
2.2.4 Steric Surface Interactions	15
2.2.5 Simulation Parameters and Boundary Conditions	16
2.3 Data Analysis	17
2.3.1 Obtaining Bacteria Number Density Maps	17
3 Heterogeneous Bacterial Densification	18
3.1 Filamentous Bacterial Densification in Flow	18
3.2 Mechanism of Densification	21

3.3	Effect of Mean Shear Rate on Densification	22
3.4	Implications of Cell Densification	23
4	Hindered Transport of Bacteria	25
4.1	Effective Bacterial Diffusion in the Absence of Shear	25
4.2	Reduced Diffusivity of Bacteria in Porous Media Flows	28
5	Conclusions and Implications	32
	References	34
	Appendix A Determination of Flow Fields within Microfluidic Porous Media	38
A.1	Particle Tracking Velocimetry Flow Field Measurements	38
A.2	Numerical Simulations of Flow Fields	38
	Appendix B Dead Cell Experiments	40
	Appendix C Ratcheting Effects in the $\theta = 7.5^\circ$ Lattice	42
	Appendix D Effect of Porosity on Bacterial Densification and Transport	44

List of figures

1.1	Motile cells in natural and engineered porous environments	2
1.2	Interactions between motile cells and the physical environment	4
2.1	Microfluidic porous medium	9
2.2	Simulation of bacterial motion	11
2.3	Unit cells for spatial averaging in 2D porous media	17
3.1	Bacterial density maps from experiments	19
3.2	Bacteria density maps from simulations	20
3.3	Role of pillars as attractors of motile cells	21
3.4	Bacterial density maps from experiments for $\theta = 0^\circ$ in various mean shear rates . .	23
3.5	Densification changes with mean shear	24
4.1	Transport of bacteria in the absence of shear.	27
4.2	Bacteria transport in the transverse flow direction for the $\theta = 0^\circ$ lattice	30
4.3	Bacterial transport in the transverse flow direction for various flow topologies (simulation)	31
A.1	Comparison of flow fields obtained from tracer particle tracking and numerical simulations in 2D and 3D	39
B.1	Particle number density maps for dead cells and microspheres in $\theta = 0^\circ$ lattice. . .	41

C.1 Ratcheting in a porous lattice with $\theta = 7.5^\circ$	43
D.1 Shear trapping at low porosity: Langevin simulations in $\theta = 0^\circ$ lattice with 0.45 porosity	45

Chapter 1

Introduction

Swimming cells, including bacteria, sperm, and plankton (Fig. 1.1 A-C), thrive in confined porous environments, often in the presence of complex fluid flows (Fig. 1.1 D-F). They are integral to numerous environmental, human health, and engineering processes including bacteria in biodegradation [19, 34, 33], sperm in reproduction [32], and microalgae in biofuel production [6]. Elucidating the mechanisms underlying the transport properties of motile cells in porous media flows is paramount to understanding and controlling these processes. In addition to the intricate pore structure and flow paths within porous media, self-propulsion, cell morphology, and the biological behaviors of swimming cells further complicate the dynamics of cell transport. Studies that consider these essential elements in describing motile cell transport in porous media are lacking. To remedy this, we use microfluidic experiments complemented by Langevin simulations to show how geometry, motility, and flow conspire to locally enhance cell concentration, while severely hindering transport coefficients of swimming bacteria in porous media flows.

Porous materials occur in many natural, biological, and engineered systems such as aquifers [16], oil reservoirs [35], tissues [27], filtration systems [62], and catalysts [49]. These materials have relatively small interconnected void spaces distributed in their structure allowing fluid to flow through them. The structure of interstices and pores in these materials can be random as in many natural systems, or ordered in well-defined lattices as in some engineered systems [20]. The pore

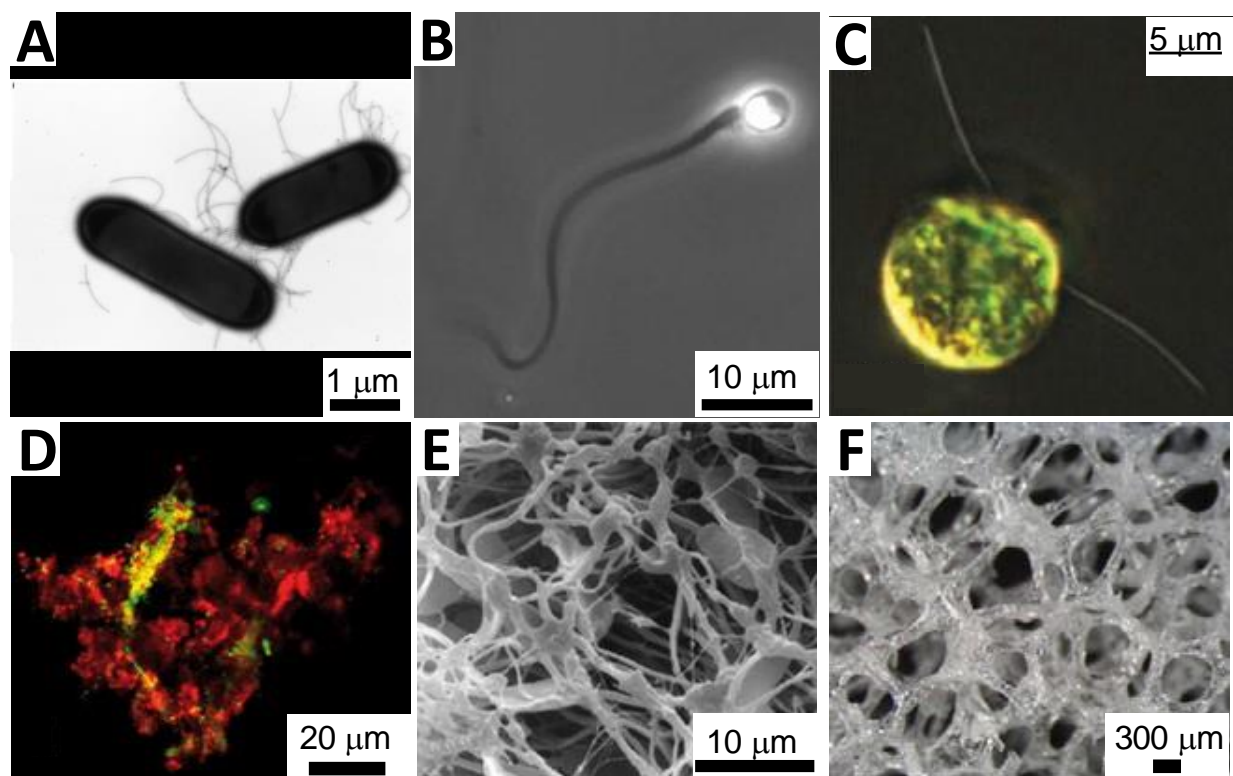


Fig. 1.1 **Motile cells in natural and engineered porous environments.** Swimming cells (top row): **A**, Multi-flagellated bacteria, *Bacillus subtilis* (credit: Grossman laboratory at MIT), **B**, human sperm (credit: J.S. Guasto), **C**, biflagellated, photosynthetic algae, *Chlamydomonas reinhardtii* (credit: K. Drescher). Porous environments (bottom row): **D**, confocal section of an organic marine aggregate (green is nucleic acid, red is glycoconjugates), **E**, bovine spermatozoa in vaginal fluid, and **F**, engineered glass sponges for light distribution in photobioreactors.

structure influences the flow and transport properties (i.e. advection and diffusion) of porous media, which are often too complicated to study in full detail, especially in randomly-structured media. While much emphasis has been placed on developing mathematical models for scalar species transport in porous media [4, 28, 17], relatively few analytical models capture the intricacies of the observed transport properties for real systems. A course-grained approach is often employed in such models to capture the dominant features, while neglecting less significant details [4, 28, 17]. A comprehensive understanding of the microscopic, pore-scale physics governing the transport of species in porous media is necessary to establish which effects may be neglected or how they may be approximated.

Arguably one of the most ecologically important species transported in porous media flows are swimming cells [2, 34, 57, 51, 22, 33, 19, 6, 29]. For example, marine bacteria thrive in porous aggregates such as marine snow and play a key role in biogeochemical cycling [2, 34]. Human parasites swim through blood flow in complex vascular networks to spread infection [57]. In the female reproductive tract motile sperm swim through biopolymer networks in cervical mucus [51] and complex tissue topology, all while subject to ciliary and peristaltic flows [22]. Swimming bacteria are used for bioremediation of oil and chemicals in aquifers [33, 19]. Microalgae cells are exposed to flow during cultivation and processing for biofuel production [6], and often utilize porous glass microstructures for light distribution and effective cell growth [29].

Self-propulsion of both prokaryotic and eukaryotic cells is conferred through thin, actuated flagella ranging in length from 5-50 μm [12]. The flagella of prokaryotic cells including bacteria (Fig. 1.1 A) are rigid, helical filaments (≈ 20 nm diameter) actuated at the base by a single rotary motor embedded in the cell membrane [8]. Eukaryotic cells including sperm (Fig. 1.1 B) and microalgae (Fig. 1.1 C) have flexible flagella (≈ 200 nm diameter), which are actuated along the length of the flagellum by dynein motors [12, 24]. These flagella are utilized in one of two general swimming styles including cells with anterior flagella that pull their bodies through fluid (e.g. microalgae) and, cells with posterior flagella that push their bodies through the fluid (e.g. bacteria and sperm) [36]. In a bulk fluid, cells often swim in persistent random walk motility patterns [10, 47, 55], where otherwise straight-line swimming is augmented by discrete, flagellar-induced turns or rotational Brownian motion [7]. While random walks of swimming cells draw comparison to the molecular diffusion of passive scalars, this analogy rapidly breaks down in non-trivial cases due to the far-from-equilibrium nature of cell motility [13].

While passive scalar and particulate transport in porous media flows are better-understood, the self-propulsion of swimming cells complicates our understanding of their transport [41, 11, 54, 37, 31, 50, 3]. Cell-surface interactions cause cells to swim along surfaces for prolonged times, including bull spermatozoa and smooth-swimming bacteria (*Escherichia coli*) that accumulate near glass surfaces (Fig. 1.2 A [41, 11]). Smooth-swimming bacteria (*E. coli*) are also trapped near

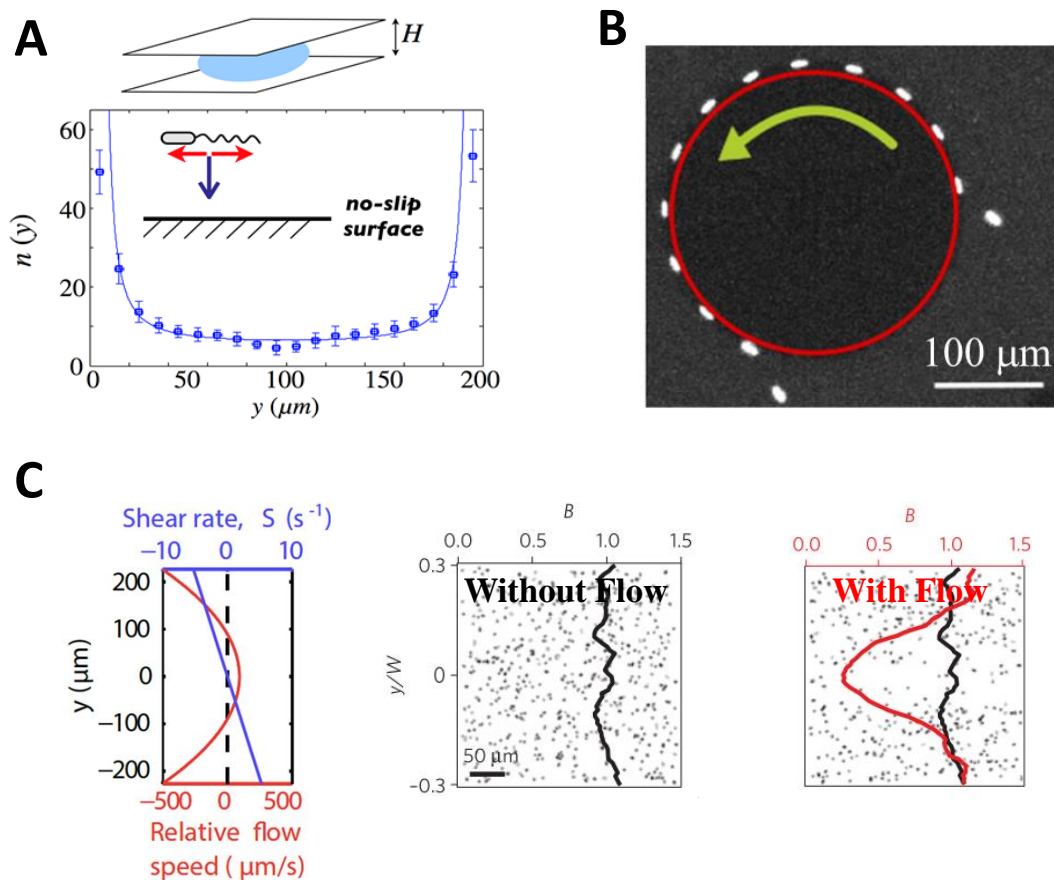


Fig. 1.2 **Interactions between motile cells and the physical environment.** **A**, Smooth-swimming *Escherichia coli* accumulate at solid surfaces due to both their hydrodynamic [11] and steric attraction to the surface. **B**, A multiple image overlay of fluorescence microscopy images of a bacterium following the curved surface of a micropillar [54]. **C**, Wild-type *Bacillus subtilis* cells have a homogeneous distribution in the absence of flow (middle). In a Poiseuille flow (left), these cells deplete from low-shear regions and accumulate in high shear regions due to their elongated shape (right). W is the width of the parabolic Poiseuille flow profile and B is the number density of bacteria [50]

microfabricated pillars of sizes in the range $20\text{-}350 \mu\text{m}$, and they orient at an angle to follow the convex curvature of pillar surfaces (Fig. 1.2 B) [54]. Both hydrodynamic and steric forces give rise to such wall-entrapment. Dipolar flow fields generated by flagellar motion induce attractive hydrodynamic forces on cells, when reflected by a wall. Moreover, cells near solid surfaces cannot easily change orientation (e.g. through tumbling) due to steric repulsion, and thus, cells spend more time swimming at the fluid-solid interface. Complex surface scattering behaviors in

phytoplankton arise from cell-surface interactions due to hydrodynamic and steric forces on actuated flagella [37, 31].

Unlike non-motile, non-Brownian particles and cells of a similar size, motility enables cells to cross fluid streamlines and generate spatially heterogeneous cell distributions [50, 3]. Elongated cell body shape, which is typical of bacteria and sperm, generates complex motility patterns in the presence of shear due to the coupling of self-propulsion and shear-induced rotation [30]. In a Poiseuille flow within a rectangular channel, swimming bacteria become trapped in high shear regions near solid boundaries leading to a heterogeneous spatial distribution of cells, which has been shown to curtail the ability of bacteria to respond to chemical gradients via chemotaxis [50] (Fig. 1.2 C). This so-called ‘shear trapping’ occurs because of the anisotropic rotation rate of elongated cells in shear due to the Jeffery orbit [30]. Bacteria rotating in Jeffrey orbits are preferentially aligned along streamlines. Thus, these cells have less time to escape from high shear regions through transverse motility, and they effectively accumulate in those high shear zones.

While significant progress has been made in recent years to understand these individual, isolated phenomena, the aggregate contribution of these mechanisms to the bulk transport properties of swimming cells in porous media is not completely clear. Different approaches exist in the study of swimming cell transport in porous media. Several works have attempted to treat bacteria as passive particles and consider mechanical dispersion to explain their transport [25, 56]. This approach ignores bacterial motility, which makes their transport properties comparable to the molecular diffusion of gasses in liquid ($D \sim 1000 \mu\text{m}^2/\text{s}$). In more recent studies, the motility of bacteria has been modeled as a diffusive process and an effective net flux has been considered for the chemotactic response of bacteria in chemical concentration gradients, when studying the transport of bacteria in a packed column [23] and a porous microchannel [38]. In those studies, the diffusion coefficient of bacteria was assumed to be altered by the tortuosity of the porous medium, and an advection-dispersion equation was used to model the transport in presence of flow. However, models that consider the coupling between bacterial motility, flow, and cell-surface interactions are lacking and the potential impacts of these effects have not been considered in porous media.

Fluid-solid interfaces and shear are inherent to porous media flows. We hypothesize that swimming cell interactions with both surfaces and shear yield spatially inhomogeneous distributions of swimming cells in porous media flows. Moreover, cells will be reorientated continuously by the shear, and also will lose their persistent swimming directions when approaching solid surfaces. The change in the persistent random walk motility of the swimming cells can alter their spreading and thus their effective diffusivity. In this work, we show, using microfluidic experiments complemented by Langevin simulations, that the complex interplay between motility, geometry, and flow leads to heterogeneous bacterial distributions and severely hindered bacterial transport properties.

Chapter 2

Microfluidic Experiments and Langevin Simulations

2.1 Model Microfluidic Porous Media and Swimming Bacteria

Microfluidic devices enable precise control over geometry and flow [60], making them an ideal platform for engineering model porous environments [38]. These devices are also highly transparent and inert, enabling unparalleled optical access for probing cell motility. We designed a microfluidic channel to elucidate the cell-scale mechanisms mediating the transport of swimming bacteria in porous media flows, which we probe using video microscopy. The simple structure of the model experimental system brings together two essential features of the porous media: hydrodynamic and solid surface interactions with swimming cells.

2.1.1 Microfluidic Device Design, Fabrication, and Characterization

The quasi-two-dimensional (quasi-2D) model microfluidic porous medium consists of a square lattice of circular pillars in a rectangular cross-section microchannel with five different angles between the mean flow direction and the lattice direction: $\theta = 0^\circ, 7.5^\circ, 15^\circ, 30^\circ, 45^\circ$ (Fig. 2.1 B). Different angles of the porous media lattices generate different flow field topologies as shown

in Fig. 2.1 C. This approach helps to minimize the vast parameter space in the design, while maintaining the periodicity of the system. The periodicity of the model enhances statistics both in experiments and simulations, by enabling periodic averaging over the spatial extent of the observable system. Moreover, periodicity eliminates mechanical dispersion in the transverse direction of the mean flow direction, enabling us to easily study the effects of the porous media flows on the effective diffusivity of the bacteria (Ch. 4). The channel has a depth, $H = 120 \mu\text{m}$, width, $W = 3.6 \text{ mm}$, and an overall length, $L = 40 \text{ mm}$, with a porous test section that is 10 mm long. The diameters of pillars are $D = 65 \mu\text{m}$ with a center-to-center distance of $d = 120 \mu\text{m}$ (i.e. edge-to-edge distance $w = 55 \mu\text{m}$). The high aspect ratio of the depth to the pore size ($H/w > 2$) ensures that the primary flow velocity gradients are in the horizontal, observation plane. In our model porous media, the size of the pores ($w = 55 \mu\text{m}$) are in the range of typical pore sizes of swimming cell environments [42](Fig. 1.1 D-E). However, the porosity of our model porous media (0.77) is high relative compared to those found in subsurface environments (e.g. aquifers and sandy soil in groundwater and hydrology studies). In Appendix D, we demonstrate the relevance of our results for other porosities.

Porous media microfluidic devices were fabricated using standard soft-lithography techniques [61]. Briefly, we prepared a casting mold by spin coating SU-8 2050 (MicroChem Corp.) on a silicon wafer and patterning the devices through photolithography using a mylar photomask (Advance Reproductions Corp.). A silicon elastomer, polydimethylsiloxane (PDMS; Dow Corning), was prepared with a 10:1 ratio by weight of polymer to cross-linker. PDMS channels were cured in an oven at 65°C for one hour, and subsequently, the PDMS channels were plasma-bonded to a standard glass microscope slide ($25 \text{ mm} \times 75 \text{ mm} \times 1 \text{ mm}$; cleaned with ethanol) [26].

2.1.2 Bacterial Cell Culturing

Wild-type *Bacillus subtilis* was chosen as a model swimming bacterium due to its average swimming speed ($V_{swim} \approx 50 \mu\text{m/s}$) and typical morphology (aspect ratio, $q \approx 10$) compared to other bacteria [50]. The bacteria were cultured by inoculating 5 mL of Cap Assay Minimal (CAM) motility medium [40] with cells obtained from a frozen glycerol stock solution. Cells were grown

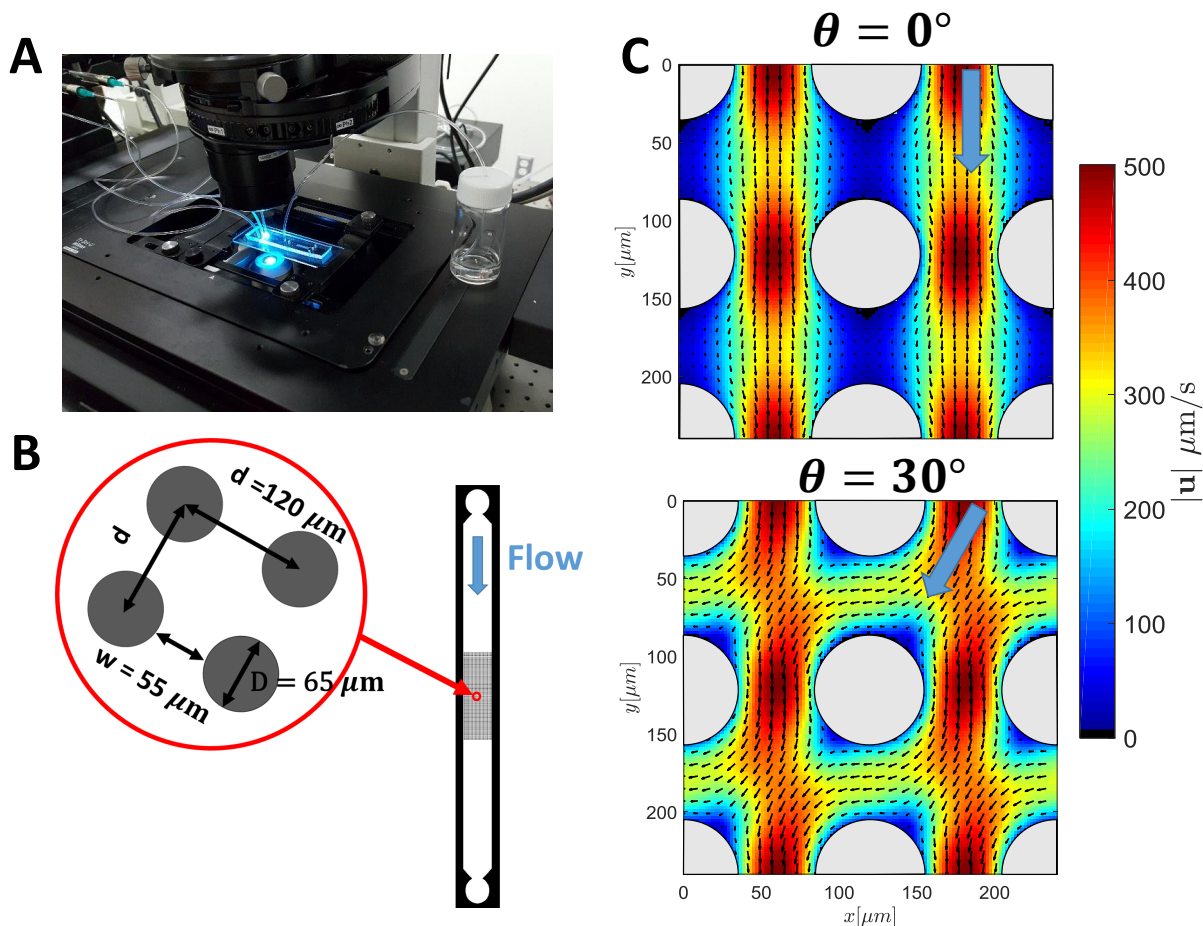


Fig. 2.1 **Microfluidic porous medium.** **A**, Experimental setup showing a microfluidic device on an inverted microscope. **B**, Schematic representation of the model porous microchannel where the lattice orientation, θ , is defined relative to the flow direction. **C**, Changing the angle of porous medium with respect to the mean flow direction modifies the flow field topology within the periodic porous medium.

overnight at 37°C while shaking at 250 rpm until the optical density reached $OD_{600} = 0.1$. 1 mL of the *B. subtilis* culture was then gently mixed with 4 mL of fresh media to obtain a sufficiently dilute suspension for cell tracking experiments.

2.1.3 Microfluidic Assays and Analyses

Bacterial suspensions were then flowed through the porous microchannels at room temperature ($\approx 22^\circ\text{C}$) with different (constant) flow rates $Q = 0, 1, 2, 3, 4, 5 \mu\text{L}/\text{min}$ using a syringe pump (PHD Ultra, Harvard Apparatus). Physically, these flow rates corresponded to mean absolute shear

rates in a range of $\bar{S} \approx U/w \approx 0 - 8 \text{ s}^{-1}$, where U is the mean flow speed ($U \approx 440 \mu\text{m/s}$ when $Q = 5 \mu\text{L/min}$). Such shear rates and flow speeds are typically observed in an array of engineering, physiological, and environmental flows [48, 52, 21, 58]. Imaging was performed in the porous test section of the channels far from the entrance pillars and bounding walls (4 lattice spacings from the end of the porous region) on an inverted microscope (Nikon Ti-E; Fig. 2.1 A). Cells were imaged using phase-contrast microscopy with a $15\times$ total magnification ($10\times$, 0.3 NA objective with a $1.5\times$ multiplier lens), and videos were recorded for 8,000 frames at 45 fps with a Zyla sCMOS camera (Andor Technology). Image analysis was performed on the videos using a custom particle tracking code written in MATLAB (MathWorks). Briefly, centroids of the bacteria were located by intensity thresholding. Next, the trajectory of each bacterium was constructed by using a predictive particle tracking algorithm [18, 15, 45]. Around 180,000 bacterial trajectories were obtained per video. This data was used to study both the population distribution and transport properties of the bacteria in our experiments. Likewise, experimental flow fields were obtained under identical conditions described above by imaging and tracking $0.5 \mu\text{m}$ diameter fluorescent tracer particles (Life Technologies). The experimental flow fields were corroborated by numerical simulations in Comsol (described below in 2.2.3).

2.2 Langevin Simulations of Bacterial Motility in Porous Media Flows

A Lagrangian model of bacterial motility was developed to capture the transport properties of swimming cells in our model porous medium. These simulations enable us to understand the observed heterogeneous densification of bacteria (Ch. 3) and to characterize their transport properties (Ch. 4). In particular, simulations complement our experiments by capturing cell trajectories over a broader range of parameters than is possible experimentally. Experiments are limited by cell trajectory length, whereby a bacterium may become occluded by a nearby pillar or its trajectory may become broken when it swims out of the focal plane.

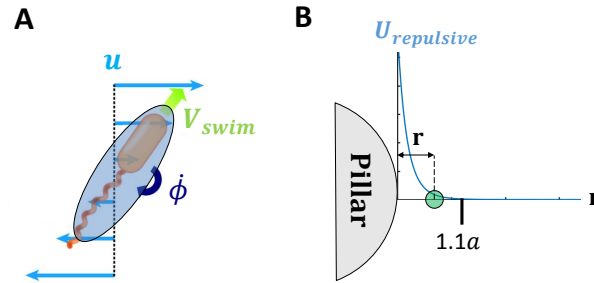


Fig. 2.2 **Simulation of bacterial motion:** **A**, Bacteria are modeled as a ellipsoids with aspect ratio q swimming along their long axis in the direction \mathbf{p} with a speed of V_{swim} and rotating at a rate of $\dot{\phi}$, which is a function of the flow field (\mathbf{u}) gradients. **B**, A repulsive potential is considered near the pillar boundaries to prevent bacteria (green circle) with an effective diameter a and center of mass at a distance r from the pillar wall from entering pillars (schematics are not to scale).

The equations of motion are developed by considering the self-propulsion of a bacterium, their translation due to advection, and their rotation due to both fluid vorticity and the coupling between the elongated cell shape and fluid extension. Fluid velocity fields were obtained by solving the Stokes equations in our porous geometry using Comsol. Due to the high aspect ratio of the channels, the equations of fluid motion were solved efficiently in 2D, and confirmed by both 3D simulations and experimentally measured flow fields by tracking $0.5 \mu\text{m}$ fluorescent particles. The bacterium is hydrodynamically approximated as a self-propelled ellipsoid with a swimming orientation along its long axis (Fig. 2.2 A). The equations for cell motion (described below) were integrated for thousands of simulated bacteria to determine the ensemble averaged steady state cell distribution as well as the effective transport coefficients for a range of flow conditions.

2.2.1 Modeling Run and Tumble Motion with Rotational Diffusion

Wild-type *Bacillus subtilis* is a peritrichously flagellated bacterium that performs a canonical ‘run-and-tumble’ swimming motility that results in a random walk trajectory. The cell ‘runs’ when all the flagellar motors rotate counterclockwise and form a bundle that propels the bacterium forward with speed $V_{swim} = 40 - 65 \mu\text{m}/\text{s}$ [40]. Stochastically one or several flagellar motors reverse their direction of rotation, where the time between reversals for a single motor is distributed exponentially yielding a mean run time of $\tau_{run} = 0.5$ s. Such reversals result in a random reorientation of the cell

or ‘tumble’, which lasts ≈ 0.1 s. In the absence of flow, the Langevin equations of motion of the center of mass of the bacterium are:

$$\dot{x} = V_{swim} \cos \phi \quad (2.1)$$

$$\dot{y} = V_{swim} \sin \phi \quad (2.2)$$

$$\dot{\phi} = f_{tumble}(t) \quad (2.3)$$

where V_{swim} is the swimming speed, ϕ is the angle of the swimming direction of the bacteria with respect to the x -axis, and f_{tumble} is a random variable chosen from the distribution of the tumble angles and described below.

The run time intervals are independent and do not depend on the previous intervals for these bacteria, resulting in their exponential distribution. We show that in this case the direction correlation function, $C(t) = \langle \mathbf{p}(0) \cdot \mathbf{p}(t) \rangle$, will decay exponentially in time with correlation (persistence) time $\tau_p = \tau_{run}/(1 - \cos(\alpha))$ where \mathbf{p} is a unit vector in the swimming direction (Fig. 2.2), τ_{run} is the mean duration of a run, and α is the mean tumble angle ($\alpha = \pi/6$ for wild-type *B. Subtilis*) [39, 50]. The distribution of the direction correlation function of a Brownian particle with a rotational diffusivity of D_{rot} also decays exponentially with a correlation time $1/D_{rot}$. Hence, the tumbling events of a bacterium can be modeled as a continuous time random walk with effective rotational diffusion of the cells $\tau_p = 1/D_{rot}$. The angular velocity $\dot{\phi}$ of a particle with a rotational diffusivity of D_{rot} is a white Gaussian noise $\xi_R(t)$ where $\langle \xi_R(t) \rangle = 0$ and $\langle \xi_R(t_1) \cdot \xi_R(t_2) \rangle = 2D_{rot} \delta(t_2 - t_1)$. Hence, we replace f_{tumble} in Eq. 2.3 with ξ_R :

$$\dot{\phi} = \xi_R \quad (2.4)$$

2.2.2 Equations of Motion of Bacteria in 2D Stokes Flow

Because bacteria live in dynamic fluid environments, we must account for the effects of advection and rotation on cell motility. The maximum Reynolds number – the ratio of inertial forces to the

viscous forces – of the cells and the channel are both sufficiently small to justify the use of the Stokes equation in modeling the flow: $Re_{cell} = Ul/\nu \sim 3 \times 10^{-3}$ and $Re_{channel} = UD_H/\nu \sim 4 \times 10^{-2}$ where U is the average flow speed ($\sim 600 \mu\text{m/s}$ for maximum simulated flow rates equivalent to $7 \mu\text{L/min}$ for experiments), l is the length of a bacterium ($10 \mu\text{m}$), D_H is the hydraulic diameter of a pore in our model porous medium that is approximately equal to the average pore spacing (ranging from $w = 55 \mu\text{m}$ to $d = 120 \mu\text{m}$), and ν is the kinematic viscosity of water ($1.004 \times 10^{-6} \text{ m}^2/\text{s}$ in the room temperature). Hence, the inertial forces on the cells are negligible compared to the viscous forces. The momentum equations for fluid flow are derived from the generalized Navier-Stokes momentum equations by neglecting the inertial terms (Stokes flow momentum equations): $\mu \nabla^2 \mathbf{v} - \nabla p + \mathbf{f} = 0$, where μ is the dynamic viscosity, \mathbf{v} is the flow velocity, p is the pressure, and \mathbf{f} is the applied body force. A nonmotile cell surrounded by the fluid, cannot exert any forces on the fluid to resist the drag forces of the flow, so it moves with the local fluid velocity in steady state:

$$\dot{x} = u_x \quad (2.5)$$

$$\dot{y} = u_y \quad (2.6)$$

where u_x and u_y are the components of the velocity field in x and y direction. Likewise, motile cells are typically modeled as hydrodynamic force dipoles, which are force and torque free. Thus, to good approximation, swimming cells also minimally disturb the flow and may be modeled as self-propelled particles whose kinematics are superimposed with the fluid flow.

In the Stokes flow regime, spherical particles rotate with an angular velocity that is equal to half of the flow vorticity, ω . However, the rotation rate of a non-spherical particle also depends on the strain rate of the flow field. *Bacillus subtilis* has an elongated shape and is composed of a $4 \mu\text{m}$ long by $1 \mu\text{m}$ diameter ellipsoidal cell body, and a $7.5 \mu\text{m}$ long helical flagellar bundle. We assume that the shape of this cell is an ellipsoid with an effective aspect ratio $q = 10$, which was previously calculated from resistive force theory [40]. The angular velocity of an ellipsoid in a 2D Stokes flow

is [46]:

$$\dot{\phi} = \frac{1}{2} \left\{ \omega + \left(\frac{1-q^2}{1+q^2} \right) \left[\sin(2\phi) \left(\frac{\partial u_x}{\partial x} - \frac{\partial u_y}{\partial y} \right) - \cos(2\phi) \left(\frac{\partial u_y}{\partial x} + \frac{\partial u_x}{\partial y} \right) \right] \right\} \quad (2.7)$$

The translational equations of motion for the bacteria are the sum of Eq. 2.1 and Eq. 2.2 with Eq. 2.5 and Eq. 2.6, respectively. The rotation rate of bacteria is obtained by adding the rotation due to effective Brownian motion (Eq. 2.4) and the rotation due to coupling to the flow gradients (Eq. 2.7):

$$\dot{x} = u_x + V_{swim} \cos(\phi) \quad (2.8)$$

$$\dot{y} = u_y + V_{swim} \sin(\phi) \quad (2.9)$$

$$\dot{\phi} = \frac{1}{2} \left\{ \omega + \left(\frac{1-q^2}{1+q^2} \right) \left[\sin(2\phi) \left(\frac{\partial u_x}{\partial x} - \frac{\partial u_y}{\partial y} \right) - \cos(2\phi) \left(\frac{\partial u_y}{\partial x} + \frac{\partial u_x}{\partial y} \right) \right] \right\} + \xi_R \quad (2.10)$$

2.2.3 Numerical Simulation of Flow through 2D Porous Media

Due to Stokes' paradox in 2D flow, analytical solutions for unbounded 2D domains are non-trivial. We used Comsol Multiphysics to solve the 2D Stokes equation numerically and obtain the flow fields required for our Langevin simulations. The geometry of the porous medium used in the numerical simulations was a 5 mm long \times 1.32 mm wide rectangle with a 11×11 square lattice of 65 μm diameter circular pillars (120 μm center-to-center pillar spacing), when the angle of the lattice with respect to the flow direction was $\theta = 0^\circ$. For lattices with $\theta \neq 0^\circ$, the square lattice of pillars was truncated to remain within the footprint of the $\theta = 0^\circ$ lattice geometry. The width and length of the channel as well as the number of pillars in the porous region were smaller in the Comsol simulation geometry compared to the experimental porous channels in order to decrease the simulation time, while increasing the resolution of the mesh. We verified that the smaller size of the computational domain as well as the 2D geometry used for obtaining the flow fields for Langevin simulations were sufficient to replicate the experimentally measured flow fields (obtained from

particle tracking data) and 3D simulations of the channel (for a single lattice angle), respectively (see Appendix A).

The simulations used a triangular mesh, which was highly refined near the pillar surfaces with a resolution of $\approx 1 \mu\text{m}$, relative to the $65 \mu\text{m}$ diameter pillars. This resolution was sufficient to resolve the high velocity gradients near the pillar surfaces. A constant upstream flow velocity of $230 \mu\text{m/s}$ was imposed at the inlet of the channel with a no-slip boundary condition on the pillar surfaces. The imposed flow speed was comparable to the experimental average flow velocity ($192 \mu\text{m/s}$) upstream of the porous test section for a flow rate $5 \mu\text{L/min}$. The flow field in the central unit cell of the porous medium lattice was extracted from the Comsol simulations for use in the Langevin simulations of bacterial motion with periodic velocity boundary conditions. The magnitude of the simulated flow field velocity was simply scaled up or down for different lattice orientations to obtain flow fields for different mean flow velocities, which is enabled by the linearity of the Stokes' equation. In Langevin simulations, the x and y components of flow velocity and their gradients at each position were obtained by interpolation of velocities in the surrounding mesh.

2.2.4 Steric Surface Interactions

The steric forces that prevent cells from penetrating pillar surfaces are modeled in a cylindrical coordinate system with a Weeks-Chandler-Andersen repulsive potential inspired from previous works (Fig. 2.2) [44]:

$$\mathbf{F}_{\mathbf{w}} = -\nabla U_{\text{repulsive}}(r) \quad (2.11)$$

$$U_{\text{repulsive}}(r) = \begin{cases} 4\epsilon \left[\left(\frac{a}{r-D/2} \right)^{12} - \left(\frac{a}{r-D/2} \right)^6 \right] + \epsilon, & r - \frac{D}{2} < 2^{1/6}a \\ 0, & r - \frac{D}{2} \geq 2^{1/6}a \end{cases} \quad (2.12)$$

where $U_{\text{repulsive}}$ is the repulsive potential, ϵ is the hardness, a is the effective radius of the cells ($\approx 3.75 \mu\text{m}$ obtained from experiments with dead cells and spherical particles; see Appendix B for more details), r is the distance of center of the sphere from the center of the pillar, and D is the

diameter of the pillar. This potential is zero when the center of the cell has a distance more than $4 \mu\text{m}$ from the pillar surfaces. Since the edge-to-edge distance of the pillars ($w = 55 \mu\text{m}$) is very large compared to this distance, it is sufficient to calculate the force from the closest pillar to the cell. At low Reynolds number, velocity is proportional to the applied force, i.e. $\mathbf{V} \sim \mathbf{F}_w/R$, where R is the resistance or drag coefficient of the particle and \mathbf{V} is its velocity.. Therefore, we can add the velocity components due to the repulsive force from the wall, $V_{x,repulsive}$ and $V_{y,repulsive}$, in Cartesian coordinate system to equations 2.8 and 2.9. Any torques from the pillar surfaces on the cells are neglected, and the ratio of ε/R is calibrated based on the time step of Langevin simulations. Thus, the complete equations of motion for the Langevin simulation of a bacterium in the model porous media flows are:

$$\dot{x} = u_x + V_{swim} \cos(\phi) + V_{x,repulsive} \quad (2.13)$$

$$\dot{y} = u_y + V_{swim} \sin(\phi) + V_{y,repulsive} \quad (2.14)$$

$$\dot{\phi} = \frac{1}{2} \left\{ \omega + \left(\frac{1-q^2}{1+q^2} \right) \left[\sin(2\phi) \left(\frac{\partial u_x}{\partial x} - \frac{\partial u_y}{\partial y} \right) - \cos(2\phi) \left(\frac{\partial u_y}{\partial x} + \frac{\partial u_x}{\partial y} \right) \right] \right\} + \xi_R. \quad (2.15)$$

2.2.5 Simulation Parameters and Boundary Conditions

About 7,000 bacteria were seeded at random positions and orientations in a unit cell, and their trajectories were obtained by numerically integrating their equations of motion with a fourth order Runge-Kutta method for 40 s with a time step of 0.01 s. The flow fields were assumed to be periodic among unit cells. We further assumed the swimming speed of the bacteria to be constant, $V_{swim} = 50 \mu\text{m/s}$, the aspect ratio to be $q = 10$, and the effective rotational diffusivity to be $D_R = 1 \text{ s}^{-1}$, similar to the parameters used in previous Langevin simulations of wild-type *Bacillus subtilis* in Poiseuille flow [50].

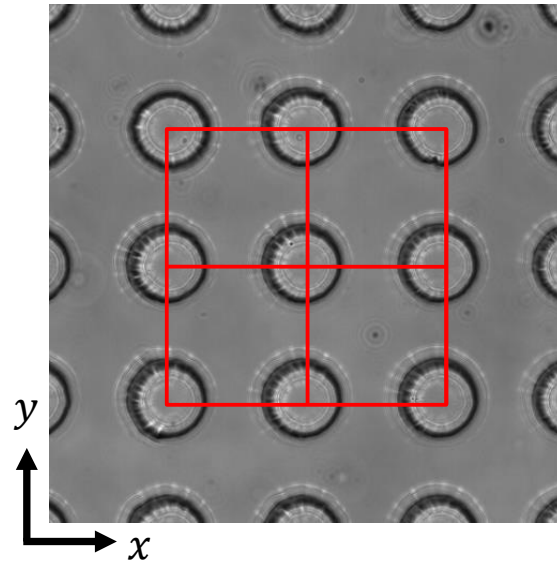


Fig. 2.3 **Unit cells for spatial averaging in 2D porous media.** Microscopy image of the pillars in the model porous microchannel. Relative positions of bacteria are found in each unit cell (red squares) to find bacterial number densities, and four of these unit cells are assembled for a better visual representation throughout the following chapters.

2.3 Data Analysis

2.3.1 Obtaining Bacteria Number Density Maps

The experimental and simulated trajectories of swimming bacteria in our model porous media quantify the spatial distribution of these cells at the pore-scale. The trajectories of bacteria include the positions of these cells in a global Cartesian coordinate system. For data analysis, the global position of each bacterium is assigned a local position within a unit cell based on the relative location of the cell from the adjacent pillars. That is, each unit cell is a $120 \mu\text{m} \times 120 \mu\text{m}$ square with its vertex on the centers of the adjacent pillars (Fig. 2.3). Binning the unit cell space and dividing the number of bacteria that have crossed each bin by the total number of observed bacteria gives the 2D bacterial number density maps. Four such unit cells are assembled for the presentation of the data.

Chapter 3

Heterogeneous Bacterial Densification

In this chapter, we study the distribution of bacteria in our model porous media and show that shear and cell-surface interactions generate heterogeneous densification of cells in porous media flows. The spatial distribution of swimming cells in their environment can impact a wide array of microbial processes including their adhesion to the surfaces, biofilm formation, and biodegradation of chemicals. Understanding the biophysical mechanisms that contribute to bacterial heterogeneity, especially in porous media, may help to elucidate fundamental processes such as niche differentiation and uptake that affect ecosystem dynamics and bioreactor efficiency. Densification may likely also result in a transient accumulation of cells, however, here we focus on the spatial distribution of the cells in the steady state.

3.1 Filamentous Bacterial Densification in Flow

In the absence of external forces, surfaces, or stimuli, bacteria are known to perform an unbiased random walk, which homogenizes their spatial distribution. In our porous microfluidic devices, the cell density is uniform far from pillars, but increases in a narrow zone near the pillar surfaces (Fig. 3.1 A). The surface accumulation of swimming bacteria is relatively well understood, and attributed to both hydrodynamic and steric cell-surface interactions. Experimentally, the optical accessibility of cells very near to the pillar surface was unreliable due to light scattering caused by

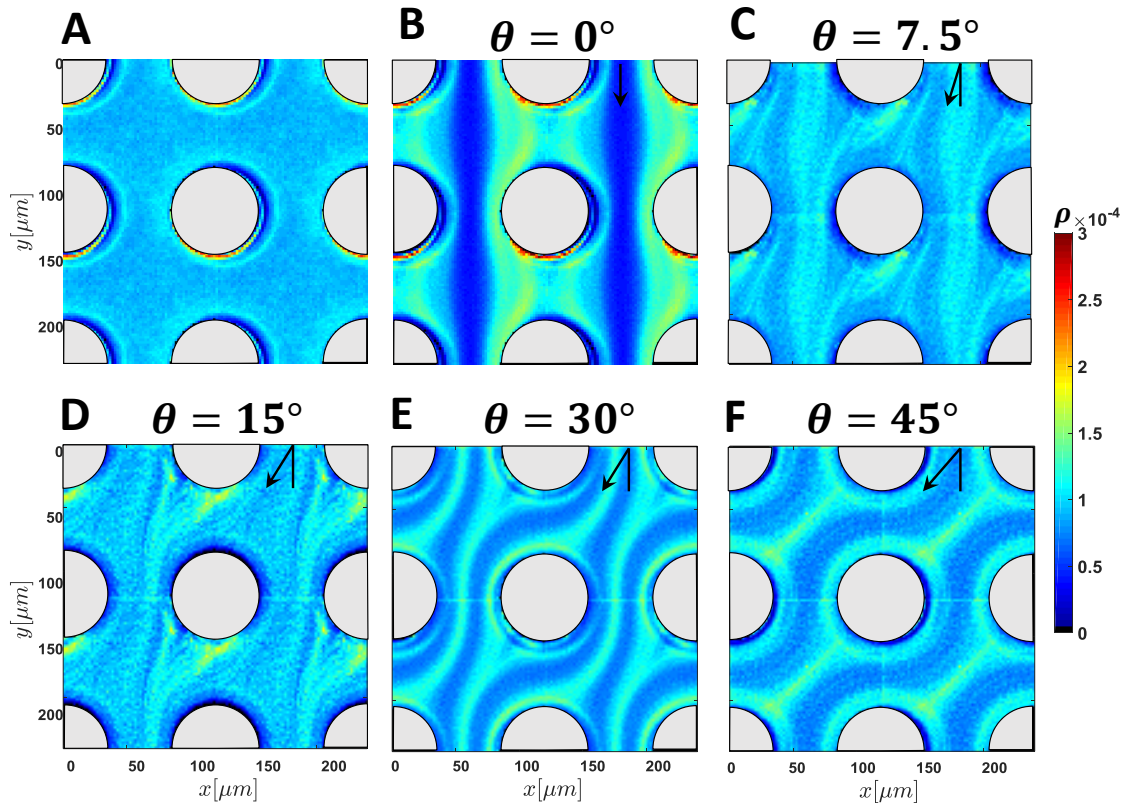


Fig. 3.1 **Bacterial density maps from experiments:** **A**, No shear. **B-F**, Mean shear rate of $\bar{S} = 5.4\text{s}^{-1}$ in lattices with different angles.

the difference in the index of the refraction of the fluid (cell culture media) and the microfluidic channel (PDMS). These unreliable near-surface regions are not considered in the analyses that follow.

In the presence of flow, the distribution of cells becomes highly heterogeneous. When the mean flow is in the lattice direction ($\theta = 0^\circ$), bacteria appear to be depleted from high fluid velocity regions, while becoming densified in low velocity regions between pillars (Fig. 3.1 B; See the corresponding flow field in Fig. 2.1 C). However, a minor change in the flow direction with respect to the pillar lattice ($\theta = 7.5^\circ$) for a fixed shear rate ($\bar{S} = 5.4\text{ s}^{-1}$) causes a drastic change in the heterogeneity (Fig. 3.1 C). We observe very fine grained filamentous patterns of cell density. Further increasing the angle of the flow results in a coarsening of the high density filaments (Fig. 3.1 D-F)

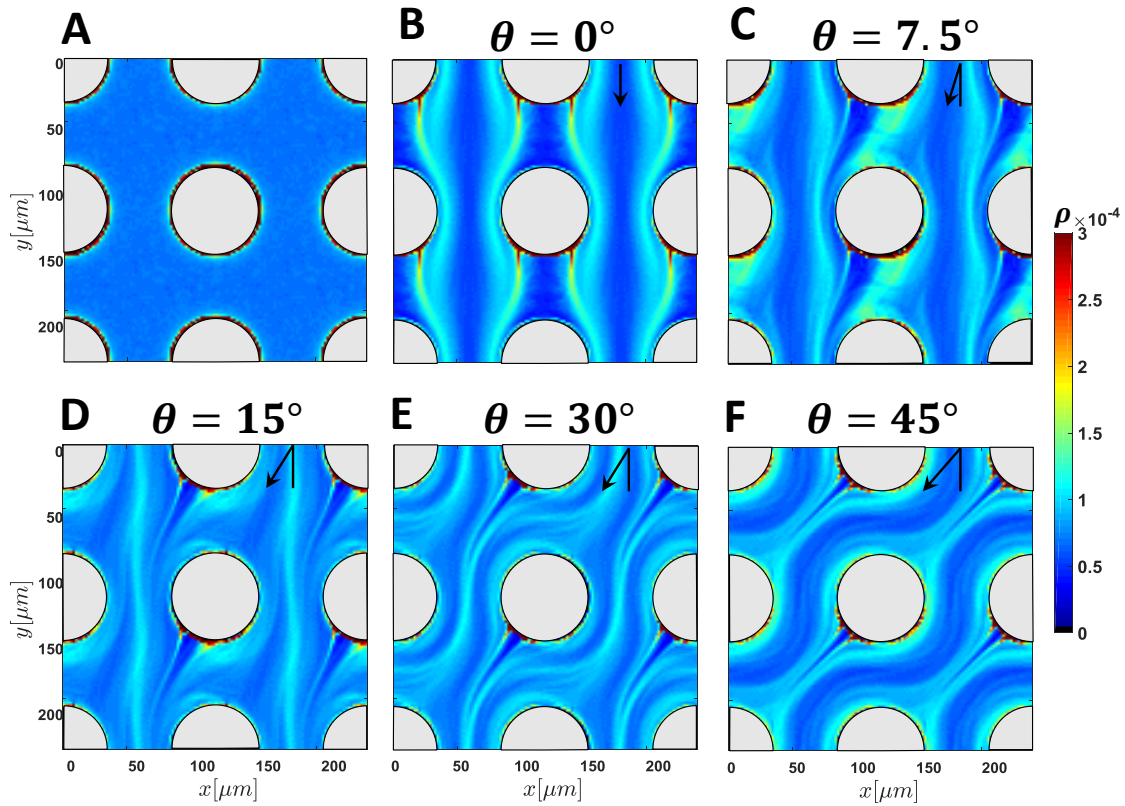


Fig. 3.2 **Bacteria density maps from simulations:** **A**, No shear. **B-F**, Mean shear rate of $\bar{S} = 5.4s^{-1}$ in lattices with different angles.

indicating that the intensity and spatial distribution of the bacteria is controlled by the flow field topology.

Langevin simulations of cell motility in porous media flows qualitatively capture the observed filamentous densification (Fig. 3.2). Using the numerical model developed in section 2.2, we determine the steady state concentration of self-propelled particles in porous media under identical conditions to the bacterial experiments described above. In the absence of flow, the cell density is homogeneous except in the areas close to the pillars (Fig. 3.2 A). The topology of the filamentous densification patterns in the presence of flow similarly captures the experimental density maps at all five flow angles (Fig. 3.2 B-F). The differences in the intensities of the bacterial number density maps of experiments and simulations could arise from several issues including: (1) using the continuous time effective rotational diffusion for the reorientation of the cells instead of an

run-and-tumble motility, (2) neglecting hydrodynamic interactions of the cells and their flagella with the pillar surfaces in the simulations, and (3) our assumption of planar bacterial motion in the experiments. However, the observed heterogeneity of the bacterial density in the porous media flows is captured by the relatively simple interplay of the physics considered in the Langevin model. In particular, the cell motility and the elongated cell shape couple to fluid flow, which are modified only by steric interactions at the solid surfaces.

3.2 Mechanism of Densification

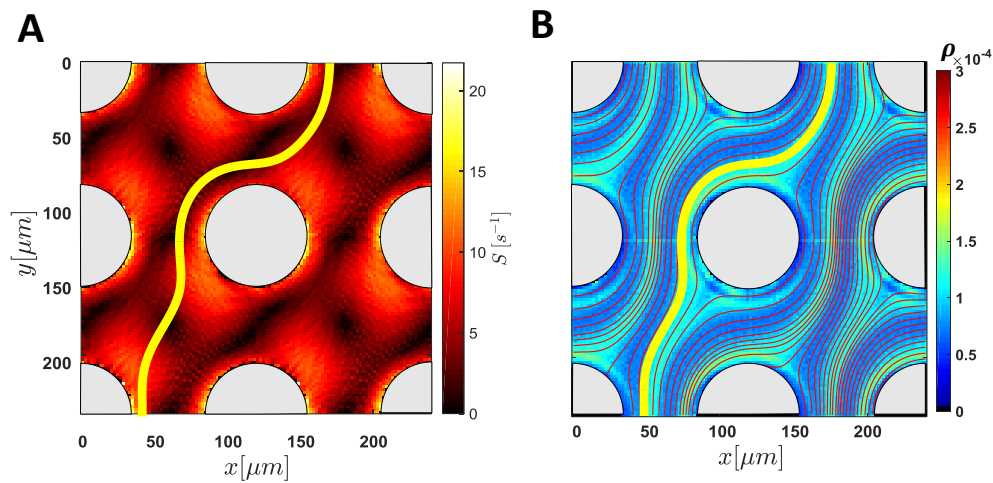


Fig. 3.3 Role of pillars as attractors of motile cells. **A**, Local shear rate computed from experimental flow fields for a flow angle of $\theta = 30^\circ$ mean shear rate $\bar{S} = 5.4s^{-1}$. Yellow curve traces a sample streamline of the flow corresponding to a high density bacterial filament. **B**, Bacteria density map with streamlines shown in red and the streamline nearest to the high density filament highlighted in yellow (corresponding to the conditions and flow in **A**).

High local shear rates are known to contribute to the densification of swimming cells by coupling the flow to cell orientation [50]. Hydrodynamic shear is a prominent feature in porous media flows due to the generation of strong velocity gradients at fluid-solid interfaces from the no-slip boundary condition. The strain rate of a flow, $\mathbf{E} = \frac{1}{2}(\nabla\mathbf{v} + \nabla\mathbf{v}^T)$, is a symmetric second-order tensor where \mathbf{v} is the local flow velocity. To correlate the hydrodynamic shear with cell densification, we quantify the magnitude of the shear rate by the maximum eigenvalue of the strain rate tensor (Fig. 3.3 A).

The magnitude of the shear is high near the pillars, again due to the no-slip boundary condition. The streamlines of the flow field in the porous microfluidic lattice with $\theta = 30^\circ$ are plotted on the corresponding bacteria density map in Fig. 3.3 B. We see that high density filamentous patterns fall onto the streamlines (e.g. yellow curve) that pass near the pillars rather than corresponding to the high shear zones in the flow field (Fig. 3.3 A). Therefore, we hypothesize that bacteria are ‘attracted’ to pillars because of cell-surface interactions (see Ch. 1) and high shear, and are then subsequently advected along the streamlines, generating the observed filamentous bacterial density patterns in the porous lattice.

3.3 Effect of Mean Shear Rate on Densification

The magnitude of the bacterial densification in the porous medium changes with the mean shear rate as the flow rate is increased. Focusing on flow along the lattice direction ($\theta = 0^\circ$), the magnitude of the bacterial densification effect appears to increase initially with increasing mean shear rate in both experiments (Fig. 3.4) and simulations (not shown). To quantify the degree of densification, we examine the probability density function (PDF) of the bacteria density in the porous lattice with $\theta = 0^\circ$ for various mean shear rates for both experiments and simulations (Fig. 3.5 A). In experiments, the locations in nearby pillars (closer than $4 \mu\text{m}$) are not considered in obtaining these PDF curves as the bacterial detection was unreliable due to the optical refraction. When $\bar{S} = 0 \text{ s}^{-1}$ the PDF is narrowly distributed (e.g. having a peak at $\rho \sim 1.4 \times 10^{-4}$ in experiments) because of the homogeneous spatial distribution of the cells in the absence of flow. As the mean shear rate increases, the PDF broadens reflecting the higher probability of more dense and less dense (depleted) regions, where the broadening is parameterized by the standard deviation, σ_{PDF} , of the PDFs. The standard deviation of the density PDFs reflects the magnitude of the densification effect in the porous environment. In the $\theta = 0^\circ$ lattice, the densification increases with mean shear rate and subsequently saturates up to $\bar{S} = 7.2 \text{ s}^{-1}$ in experiments (Fig. 3.5 B), but decreases in the highest shear rate. The saturation is consistent with previous measurements of bacterial trapping in

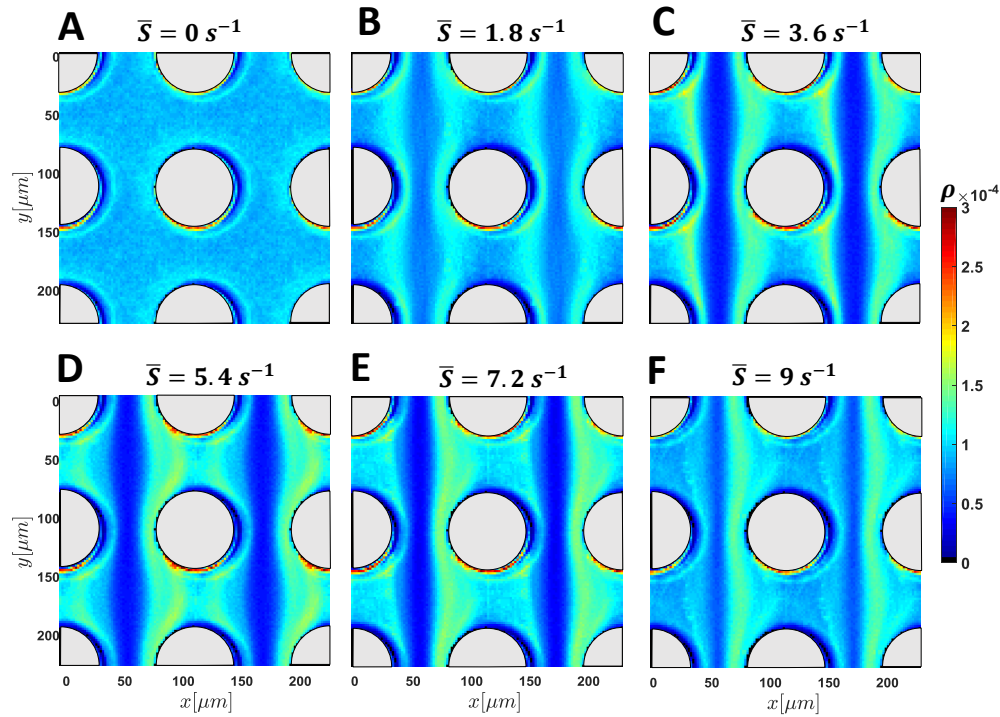


Fig. 3.4 **Bacterial density maps from experiments for $\theta = 0^\circ$ in various mean shear rates. A-F** Bacterial density maps for mean shear rates \bar{S} from 0 to 9 s^{-1} .

a Poiseuille flow through a rectangular channel [50] that showed a maximum in the densification for the shear rates in the range explored here. Simulations enable the efficient exploration of the trapping strength for a broader range of shear rates and reflect the saturation of densification in the lattices with $\theta = 0^\circ$ and $\theta = 30^\circ$ (Fig. 3.5 C).

3.4 Implications of Cell Densification

In addition to physical effects on bacterial transport in porous media, the local densification of cells in the system described here has wide-ranging ecological and evolutionary implications for microbes. The collocation of osmotrophic cells with dissolved resources could lead to niche partitioning on evolutionary time scales whereby cells evolve to take advantage of a locally abundant resource apart from other competing organisms. Conversely, the coupling of the physical environment to cell motility may adversely affect cells by ‘shear trapping’ in porous media that deprive cells of

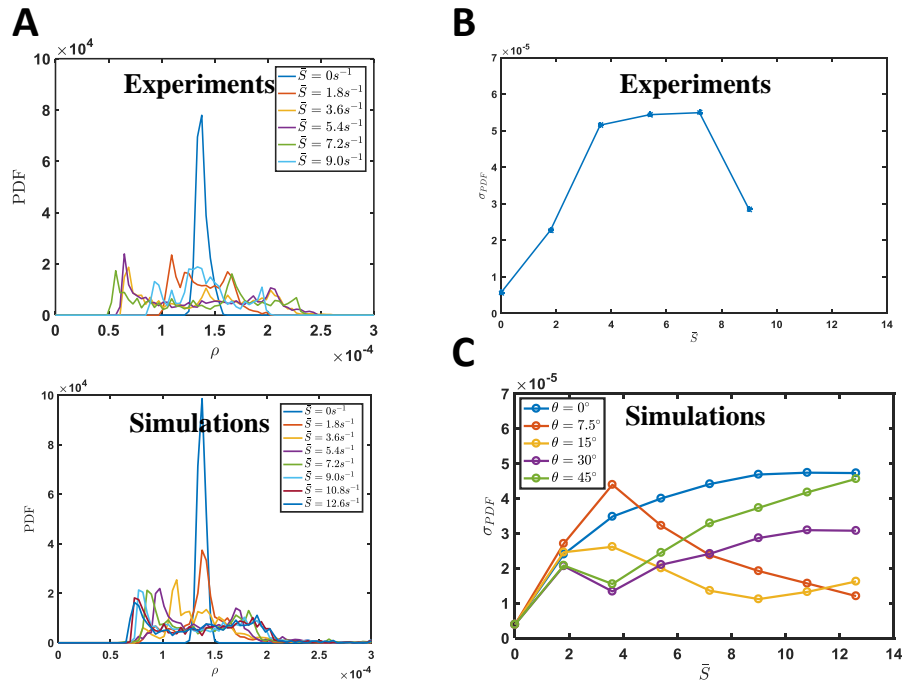


Fig. 3.5 **Densification changes with mean shear.** **A** Probability density function from the experimental (top) and simulated (bottom) bacterial density maps for the $\theta = 0^\circ$ lattice and for various mean shear rates. **B** Standard deviation of the PDF curves show a maximal trapping for intermediate shear rates \bar{S} for the experimental density maps in $\theta = 0^\circ$ lattice. **C** Simulations enable the efficient exploration of the trapping strength for a broader range of shear rates and for all lattice angles.

nutrient uptake in dynamic ecosystems and biomes. More specifically, suspensions of high aspect ratio bacteria are observed to be retained when flowed through packed quartz sands as compared to lower aspect ratio cells [59]. The trapping phenomenon observed in our work likely resolves this long-unexplained observation of the retention of elongated bacteria in porous media flows.

Chapter 4

Hindered Transport of Bacteria

The canonical random walk motility of bacteria has long-motivated the extension of advection-diffusion models to bacterial transport in porous media flows, analogous to solute dispersion through an assumed constant effective diffusion coefficient for the bacteria [38, 43]. However, we show that this analogy breaks down as the effective diffusion coefficient of the bacteria decreases rapidly with increasing flow through the porous medium. While bacteria spread in both the longitudinal and transverse directions with respect to the mean flow direction, the former is dominated by dispersion effects. Focusing on the transverse direction to the flow, we take advantage our robust Langevin simulation data to study the effective transport coefficients of bacteria, and later, compare these results with experiments.

4.1 Effective Bacterial Diffusion in the Absence of Shear

Swimming bacteria perform a persistent random walk in a quiescent fluid, where the random walk is known to result in diffusive transport for times longer than the persistence time ($\tau_p = 1$ s) of the cell orientation [39, 7]. In simulations without flow, the probability distributions of bacterial displacements, $p(\Delta x, \Delta t)$, exhibit a non-Gaussian shoulder for short times, when displacements are small compared to both the swimming persistence length of the cells $l_p = V_{swim} \tau_p \sim 50 \mu\text{m/s} \times 1 \text{ s} \sim 50 \mu\text{m}$ and to the lattice spacing $s = 120 \mu\text{m}$, i.e. $\Delta x < l_p < s$ (Fig. 4.1 A). However, the

displacement distributions evolve into Gaussian shapes (parabolic on semi-log scale) for longer times, a usual indicator of diffusive transport. For these long times, the mean squared displacements (MSD) of bacteria increase linearly with time, $\text{MSD}_\perp(t) = \langle (x(t) - x(0))^2 \rangle = 2D_\perp(t - \alpha\tau_p)$, where D_\perp is the effective diffusion coefficient of bacteria in the transverse direction and $\alpha\tau_p$ is the offset due to the non-diffusive motion of the bacteria in short times (Fig. 4.1 B).

The diffusive behavior of the self-propelled particles, which arises from their intrinsic random walk properties, is encapsulated in the correlation function of their swimming velocity:

$$\Psi(t) = \langle \mathbf{v}(t) \cdot \mathbf{v}(0) \rangle, \quad (4.1)$$

where \mathbf{v} is the velocity of a bacterium and $\langle \cdot \rangle$ denotes ensemble averaging. Even though self-propelled particles will diffuse fast if they swim with a high velocity, the time that they spend swimming in a specific direction is also important. For instance, smooth-swimming *B. subtilis* have a similar swimming speed to wild-type cells, but do not perform a run-and-tumble motion. They spend more time swimming along an initial direction, so their effective diffusion coefficient is larger than corresponding wild-type (i.e. run-and-tumble) strains. The swimming direction of smooth-swimming cells changes because of a small, random, rotational diffusion that stems from both Brownian rotational diffusion and intrinsic noise in their flagellar propulsion system [9]. While the duration of a run is important, the tumbling angle is also a key parameter in characterizing the diffusion of the bacteria. If bacteria tumble with a smaller angle, they will tend to exhibit a higher persistence (see section 2.2.1) and thus, higher effective diffusivity.

From the Green-Kubo expression, the effective diffusion coefficient of the bacteria is equal to the integral of the correlation function of the cell velocity over time,

$$D = N_D \int_0^\infty \langle \mathbf{v}(t) \cdot \mathbf{v}(0) \rangle dt \quad (4.2)$$

where N_D is the spatial dimension of the random walk: $N_D = 1$ for 1D swimming on a line, $N_D = 2$ for 2D swimming in a plane, and $N_D = 3$ for 3D swimming in bulk. In a quiescent fluid, the model

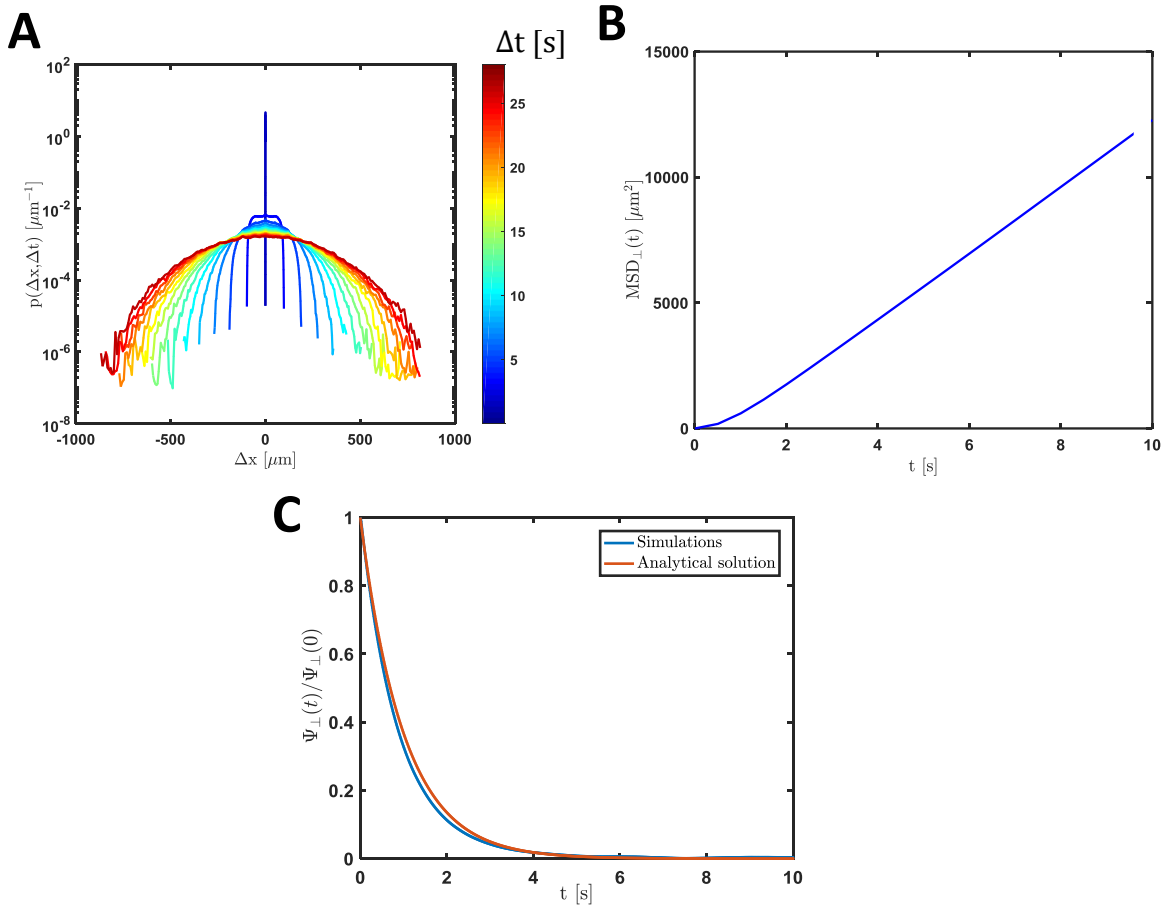


Fig. 4.1 **Transport of bacteria in the absence of shear.** **A**, Probability distributions of bacterial displacements evolve into Gaussian shapes (parabolic in semi-log scale), when displacements are larger than the persistence length of bacteria and the pillar spacing of the porous medium. **B**, Mean squared displacements (MSD) of bacteria show a diffusive motion for times longer than the persistence time of swimming, $\tau_p = 1$ s. **C**, Normalized velocity correlation function of bacteria in the transverse direction of the flow decreases exponentially with time. The decay is faster in simulations having pillars (blue curve) as compared to the analytical solution (red curve) in a bulk fluid. The x -axis is transverse to the flow direction.

wild-type *Bacillus subtilis* bacterium swims with a constant swimming speed, and the swimming velocity is then $\mathbf{v}(t) = V_{swim}\mathbf{p}(t)$, where \mathbf{p} is the swimming direction (Fig. 2.2 A). In this case, the velocity correlation of the bacterium is:

$$\Psi(t) = V_{swim}^2 \langle (\mathbf{p}(t) \cdot \mathbf{p}(0)) \rangle = V_{swim}^2 C(t) \quad (4.3)$$

$C(t)$ is the direction correlation function of our model swimmer in a quiescent flow and as discussed previously (section 2.2.1), it decays exponentially with a persistence time τ_p :

$$C(t) = e^{-t/\tau_p}. \quad (4.4)$$

Using Eq. 4.2, 4.3, and 4.4, the expression for the effective diffusion coefficient of the bacteria in a quiescent fluid is:

$$D = \frac{V_{swim}^2}{N_D D_{rot}}. \quad (4.5)$$

Setting $V_{swim,\perp} = 50/\sqrt{2} \mu\text{m/s}$, $D_{rot} = 1 \text{ s}^{-1}$, and $N_D = 1$ for transverse direction, the effective diffusion coefficient of the bacteria will be $D_{\perp} = 1250 \mu\text{m}^2/\text{s}$. However, in the porous media, the presence of the pillars decreases the persistence swimming time of the bacteria. Thus, $\Psi_{\perp}(t)/\Psi_{\perp}(0)$, where Ψ_{\perp} is the velocity correlation in the transverse flow direction, decays slightly faster in the simulations than the analytical solution for the swimming bacteria in bulk fluid (Eq. 4.4 when $\tau_p = 1$ s), which reduces the diffusion coefficient to $D_{\perp} = 980 \mu\text{m}^2/\text{s}$ (Fig. 4.1 C). The altered diffusion of bacteria in the presence of impermeable grains is in general agreement with previous studies [23].

4.2 Reduced Diffusivity of Bacteria in Porous Media Flows

In the presence of flow, the transport of the bacteria in the $\theta = 0^\circ$ lattice is diffusive in the transverse flow direction as their mean squared displacements evolve linearly with slope unity in log-scale (Fig. 4.2). Straight lines were fitted to the MSD curves for times longer than 20 s (10 points) to calculate the effective diffusion coefficient of bacteria for each shear rate (equal to half of the slope of MSD curve). The effective diffusion coefficient of the bacteria decreases rapidly with increasing mean shear rate (Fig. 4.2 B).

The altered diffusion coefficient of the bacteria is better understood in terms of the decorrelation of their velocities over time. The normalized velocity correlations in the presence of shear for the

$\theta = 0^\circ$ porous lattice decay faster than the correlation function in the absence of flow (Fig. 4.2 C). In the absence of shear and steric interactions, the bacterial velocity decorrelates exponentially as it is coupled to the cell orientation whose speed changes randomly (modeled as a white Gaussian noise; see Eq. 2.3 and 2.4; Fig. 4.1 C). However, in a porous media flow, the bacterial velocity (and orientation) is coupled to the steric forces, advection, and fluid rotation through the flow gradients (i.e. shear). This complicates the dynamics of the swimmers and their velocities through time (Eq. 2.13 - 2.15). In particular, the added rotation due to the flow gradients (i.e. Jeffery orbits) causes the velocities of self-propelled particles to decorrelate faster. The effective diffusion coefficients are calculated using the Green-Kubo expression, and closely match the diffusion coefficients obtained from fitting the MSD curves (Fig. 4.2 B).

The Green-Kubo expression is more suitable than MSDs and probability distributions of displacements to characterize the transport of live bacteria from the short experimental trajectories as it links short-term dynamics of the swimmer to the long term transport properties. Figure 4.2 D shows the normalized velocity correlation functions from experimental trajectories that capture strong, nearly exponential decay of the effective diffusion coefficient with increasing shear observed in simulations (Fig. 4.2 C). The effective diffusion coefficients of bacteria are calculated by integrating the experimental velocity correlation curves (Fig. 4.2 B). The decrease in the effective diffusion coefficients of bacteria is observed for mean shear rates up to $\bar{S} = 3.6 \text{ s}^{-1}$. However, the effective diffusion coefficient increases with further increasing mean shear rate in experiments. We believe that this latter behavior is unphysical due to the lack of robust measured cell trajectories at such high flow speeds. That is, increasing the flow speed leads to more mis-tracking events and decreases the number of reliable long trajectories, thus causing errors that propagate into the integration of the velocity autocorrelations.

Suppression of the bacterial transport coefficients with increasing mean shear rate is generally observed in other porous media flow field topologies as well (Fig. 4.3). Steric interactions are known to lead to ballistic transport through a 'ratcheting' effect, which was observed in the $\theta = 7.5^\circ$ lattice and subtracted from cell motion when computing the effective transport coefficients (see

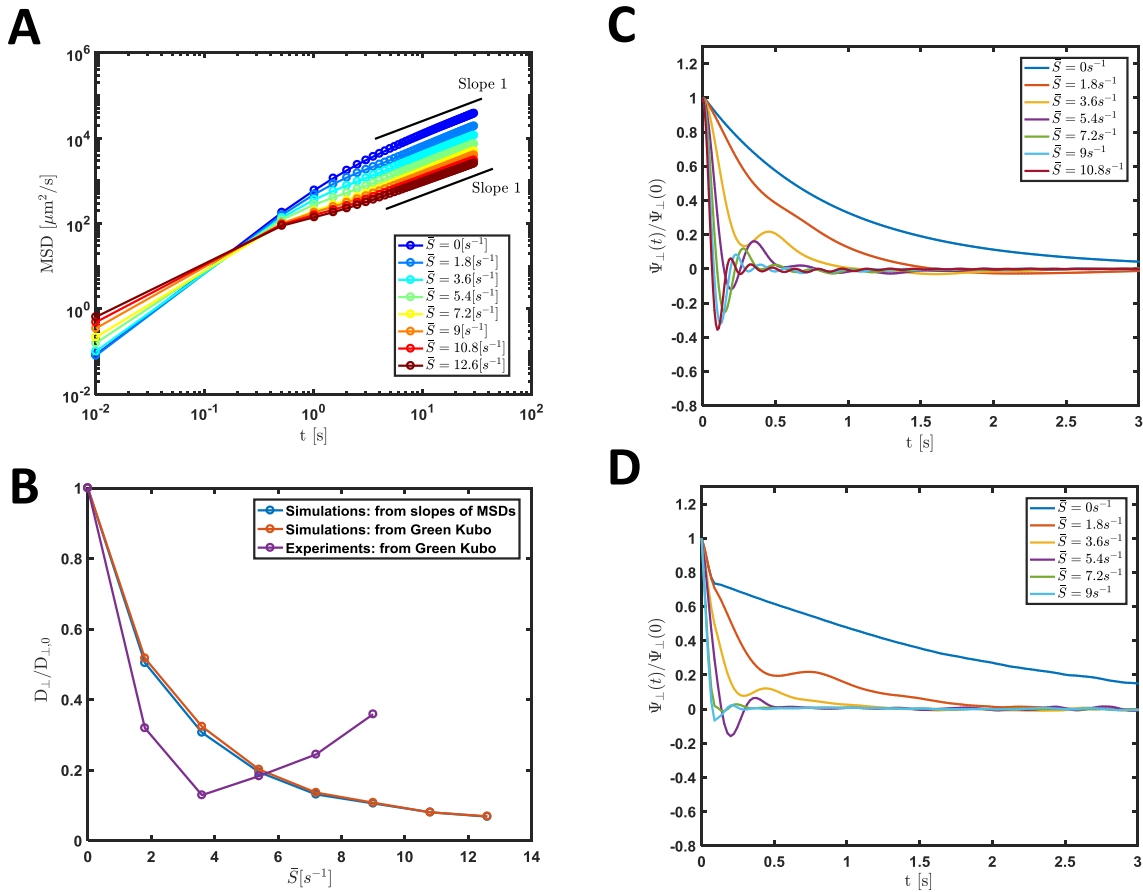


Fig. 4.2 **Bacteria transport in the transverse flow direction for the $\theta = 0^\circ$ lattice.** **A**, Mean squared displacements of bacteria in the transverse flow direction (MSD_\perp) show diffusive transport for long times as their slopes tend to unity in log-scale. The offsets between the curves show the hindered diffusion of the bacteria in the presence of increasing shear. **B**, The effective diffusion coefficients of the bacteria (D_\perp) in the transverse flow direction normalized by the effective diffusion coefficient in the absence of shear ($D_{\perp,0}$). Transport coefficients decrease rapidly with increasing mean shear rate. Suspected experimental tracking errors cause deviations from this behavior for measured transport coefficients at high shear. **C**, Velocity correlation functions of bacteria obtained from the Langevin simulations decay faster in presence of shear. **D**, Velocity correlation functions of the bacteria obtained from the experiments capture the basic features of the velocity correlations obtained from the simulations in C, showing fast decays with increased shear.

Appendix C for more details). The altered effective diffusivity of bacteria in various flow field topologies in our model porous media suggests that this phenomenon happens in most porous media as we showed the importance of advection, flow gradients, and steric interactions that alter the velocity correlations of the bacteria.

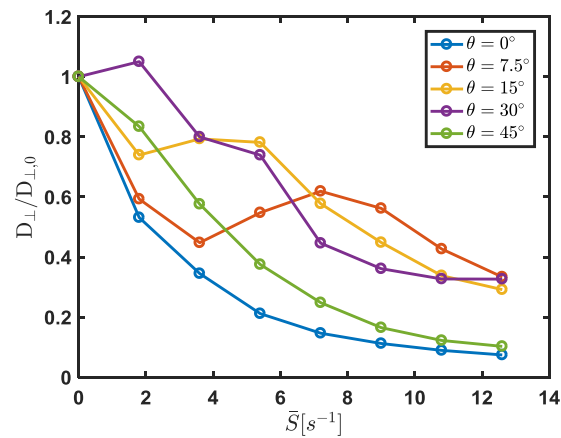


Fig. 4.3 **Bacterial transport in the transverse flow direction for various flow topologies (simulation)** The effective diffusion coefficients of bacteria (D_{\perp}) normalized by the effective diffusion coefficients in the absence of shear ($D_{\perp,0}$) in the transverse direction. The presence of shear in porous media generally decreases the effective diffusion coefficients of the bacteria in square porous lattices for all flow topologies examined (i.e. various flow angles relative to the lattice direction).

Chapter 5

Conclusions and Implications

The work presented here unequivocally illustrates that fluid flows through porous media couple to cell shape and motility to locally augment their concentration and inhibit transport. Our microfluidic experiments in model porous media, complemented by simulations, demonstrated that the local density of cells may be greatly enhanced by the presence of hydrodynamic shear, which is ever present in flow near fluid-solid interfaces in porous media. The preferential alignment of cells relative to the near-surface shear and steric rectification of cells at solid surfaces contributes to the formation of filamentous structures of high bacterial concentration. We demonstrated that shear also contributes strongly to the decorrelation of bacterial swimming causing a dramatic decrease of the effective bacterial transport coefficients with increasing ambient shear. Strikingly, the local densification of cells depends strongly on cell shape through Jeffery orbits, where elongated cells become densified and spherical cells sample space more uniformly. Conversely, shear ubiquitously hinders swimming cell transport irrespective of cell shape. The non-linear effect of the shear on the effective diffusion coefficients of the bacteria suggests that the linear superposition of advection and diffusion is insufficient to predict cell transport in porous media flows.

Bacteria are well known to play important roles in a range of ecological and industrial processes in porous media. The resulting heterogeneous distribution of cells at the pore scale has the potential to impact a broad array of microbial functions and biome dynamics. Our results suggest that the

observed bacterial trapping may promote cell adhesion and subsequent biofilm formation in porous media, as bacteria tend to accumulate in high shear regions at fluid-solid interfaces. In a similar way, the induced bacterial heterogeneity may severely diminish or enhance the uptake of nutrients or the reception of chemical signals, depending upon the relative location of the dissolved solutes. The local densification of cells will result in local competition for dissolved resources, and could inhibit uptake if the resources are not co-located in the densified cell regions. Conversely, phenotypically different species having various morphologies or swimming kinematics may become densified in disjoint regions of the porous medium, potentially reducing competition for specific resources. Over evolutionary time scales, cells may evolve with resource specificity, resulting in niche partitioning among species. Furthermore, heterogeneous flow tends to promote mixing of passive scalars such as nutrients or chemical signal in porous media, similar to turbulent flows, making patches of dissolved resources highly ephemeral. Inhibition of bacterial transport coefficients will likely reduce their chemotactic ability, and thus the efficacy with which they take advantage of such ephemeral resources. The impact of flow on cell transport demonstrated here will undoubtedly lead to new discoveries in the physical ecology of biomes, the impact of the physical environment on evolution, and a better understanding for bioengineering of industrial systems.

References

- [1] Al-Raoush, R. and Willson, C. (2005). Extraction of physically realistic pore network properties from three-dimensional synchrotron X-ray microtomography images of unconsolidated porous media systems. *Journal of Hydrology*, 300(1-4):44–64.
- [2] Azam, F., Fenchel, T., Field, J. G., Gray, J. C., Meyer-Reil, L. A., and Thingstad, F. (1983). The ecological role of water-column microbes in the sea. *Marine Ecology Progress Series*, 10(3):257–263.
- [3] Barry, M. T., Rusconi, R., Guasto, J. S., and Stocker, R. (2015). Shear-induced orientational dynamics and spatial heterogeneity in suspensions of motile phytoplankton. *J R Soc Interface*, 12(112).
- [4] Bear, J. and Bachmat, Y. (1990). *Introduction to Modeling of Transport Phenomena in Porous Media*. Springer Netherlands, Dordrecht, 1 edition.
- [5] Beech, J. (2011). *Microfluidics Separation and Analysis of Biological Particles*. PhD thesis, Lund University.
- [6] Bees, M. A. and Croze, O. A. (2014). Mathematics for streamlined biofuel production from unicellular algae. *Biofuels*, 5(1):53–65.
- [7] Berg, H. C. (1993). *Random walks in biology*. Princeton University Press.
- [8] Berg, H. C. (2003). The rotary motor of bacterial flagella. *Annual review of biochemistry*, 72(1):19–54.
- [9] Berg, H. C. (2004). *E. Coli in Motion*. Springer-Verlag New York, 1 edition.
- [10] Berg, H. C. and Brown, D. a. (1972). Chemotaxis in *Escherichia coli* analysed by three-dimensional tracking. *Nature*, 239(5374):500–504.
- [11] Berke, A. P., Turner, L., Berg, H. C., and Lauga, E. (2008). Hydrodynamic attraction of swimming microorganisms by surfaces. *Physical Review Letters*, 101(3).
- [12] Brennen, C. and Howert Winet (1977). Fluid Mechanics of Propulsion By Cilia and Flagella. *Annual Review of Fluid Mechanics*, 9(Lehninger 1971):339–398.
- [13] Cates, M. E. (2012). Diffusive transport without detailed balance in motile bacteria: does microbiology need statistical physics? *Reports on progress in physics. Physical Society (Great Britain)*, 75(4):042601.
- [14] Chao, Y. and Zhang, T. (2011). Optimization of fixation methods for observation of bacterial cell morphology and surface ultrastructures by atomic force microscopy. *Applied Microbiology and Biotechnology*, 92(2):381–392.

- [15] Cheezum, M. K., Walker, W. F., and Guilford, W. H. (2001). Quantitative comparison of algorithms for tracking single fluorescent particles. *Biophysical journal*, 81(4):2378–2388.
- [16] Cherry, J., Gillham, R., Sudicky, E., and MacFarlane, A. (1983). MIGRATION OF CONTAMINANTS IN GROUNDWATER AT A -' NDFILL: A CASE STUDY houndwater Flow and Plume Delineation. *Journal of Hydrology J. Hydrol*, 6(63):3–1.
- [17] Civan, F. (2011). *Porous Media Transport Phenomena*.
- [18] Crocker, J. C. and Grier, D. G. (1996). Methods of Digital Video Microscopy for Colloidal Studies. *Journal of Colloid and Interface Science*, 179(1):298–310.
- [19] Das, K. and Mukherjee, A. K. (2007). Crude petroleum-oil biodegradation efficiency of *Bacillus subtilis* and *Pseudomonas aeruginosa* strains isolated from a petroleum-oil contaminated soil from North-East India. *Bioresource Technology*, 98(7):1339–1345.
- [20] Davis, M. E. (2002). Ordered porous materials for emerging applications. *Nature*, 417(6891):813–821.
- [21] Eytan, O., Jaffa, A. J., and Elad, D. (2001). Peristaltic flow in a tapered channel: application to embryo transport within the uterine cavity. *Medical Engineering & Physics*, 23:473–482.
- [22] Fauci, L. J. and Dillon, R. (2006). Biofluidmechanics of Reproduction. *Annual Review of Fluid Mechanics*, 38(1):371–394.
- [23] Ford, R. M. and Harvey, R. W. (2007). Role of chemotaxis in the transport of bacteria through saturated porous media. *Advances in Water Resources*, 30(6-7):1608–1617.
- [24] Goldstein, R. E. (2015). Green Algae as Model Organisms for Biological Fluid Dynamics. *Annual review of fluid mechanics*, 47:343–375.
- [25] Harvey, R. W. and Garabedian, S. P. (1991). Use of Colloid Filtration Theory in Modeling Movement of Bacteria through a Contaminated Sandy Aquifer. *Published in Environmental Science & Technology*, pages 178–185.
- [26] Haubert, K., Drier, T., Beebe, D., Duffy, D., McDonald, J., Schueler, O., Whitesides, G., Jo, B., Lerbeergh, L. V., Motsegood, K., Beebe, D., Ginn, B., Steinbock, O., Eddington, D., Puccinelli, J., and Beebe, D. (2006). PDMS bonding by means of a portable, low-cost corona system. *Lab on a Chip*, 6(12):1548.
- [27] Hollister, S. J. (2005). Porous scaffold design for tissue engineering. *Nature materials*, 4(July):518–24.
- [28] Ichikawa, Y. and Selvadurai, A. (2012). *Transport Phenomena in Porous Media*. Springer Berlin Heidelberg, Berlin, Heidelberg.
- [29] Jacob, A., Bucharsky, E. C., and GuenterSchell, K. (2012). The Application of Transparent Glass Sponge for Improvement of Light Distribution in Photobioreactors. *Journal of Bioprocessing & Biotechniques*, 02(01):1–8.
- [30] Jeffery, G. B. (1922). The Motion of Ellipsoidal Particles Immersed in a Viscous Fluid. *Proceedings of the Royal Society of London. Series A*, 102(715):161 LP – 179.

- [31] Kantsler, V., Dunkel, J., Blayney, M., and Goldstein, R. E. (2014). Rheotaxis facilitates upstream navigation of mammalian sperm cells. *eLife*, 3:e02403.
- [32] Kaupp, U. B., Kashikar, N. D., and Weyand, I. (2008). Mechanisms of sperm chemotaxis. *Annual review of physiology*, 70:93–117.
- [33] Khan, F. I., Husain, T., and Hejazi, R. (2004). An overview and analysis of site remediation technologies.
- [34] Kirchman, D. L. (2008). New light on an important microbe in the ocean. *Proceedings of the National Academy of Sciences of the United States of America*, 105(25):8487–8488.
- [35] Kavscek, A. R., Wong, H., and Radke, C. J. (1993). A pore level scenario for the development of mixed wettability in oil reservoirs. *AIChE Journal*, 39(6):1072–1085.
- [36] Lauga, E. and Powers, T. R. (2009). The hydrodynamics of swimming microorganisms. *Rep. Prog. Phys.* *Rep. Prog. Phys.*, 72(72):96601–36.
- [37] Li, G. and Tang, J. X. (2009). Accumulation of microswimmers near a surface mediated by collision and rotational Brownian motion. *Physical Review Letters*, 103(7).
- [38] Long, T. and Ford, R. M. (2009). Enhanced transverse migration of bacteria by chemotaxis in a porous T-sensor. *Environmental Science and Technology*, 43(5):1546–1552.
- [39] Lovely, P. S. and Dahlquist, F. W. (1975). Statistical measures of bacterial motility and chemotaxis. *Journal of Theoretical Biology*, 50(2):477–496.
- [40] Marcos, Fu, H. C., Powers, T. R., and Stocker, R. (2012). Bacterial rheotaxis. *Proceedings of the National Academy of Sciences of the United States of America*, 109(13):4780–5.
- [41] Maude, a. D. and ROTHSCILD (1963). Non-Random Distribution of Bull Spermatozoa in a Drop of Sperm Suspension. *Nature*, 198(4886):1221–1222.
- [42] Nimmo, J. R. (2004). Porosity and Pore Size Distribution. (3):295–303.
- [43] Olson, M. S., Ford, R. M., Smith, J. A., and Fernandez, E. J. (2006). Mathematical Modeling of Chemotactic Bacterial Transport through a Two-Dimensional Heterogeneous Porous Medium. *Bioremediation Journal*, 10(12):13–23.
- [44] Ostapenko, T., Schwarzendahl, F., B öddeker, T., Kreis, C., Cammann, J., Mazza, M. G., and Bäumchen, O. (2016). Curvature-guided motility of microalgae in geometric confinement. *eprint arXiv:1608.00363*, pages 1–8.
- [45] Ouellette, N. T., Xu, H., and Bodenschatz, E. (2006). A quantitative study of three-dimensional Lagrangian particle tracking algorithms. *Experiments in Fluids*, 40(2):301–313.
- [46] Parsa, S., Guasto, J. S., Kishore, M., Ouellette, N. T., Gollub, J. P., and Voth, G. a. (2011). Rotation and alignment of rods in two-dimensional chaotic flow. *Physics of Fluids*, 23(4):043302.
- [47] Polin, M., Tuval, I., Drescher, K., Gollub, J. P., and Goldstein, R. E. (2009). Chlamydomonas swims with two "gears" in a eukaryotic version of run-and-tumble locomotion. *Science (New York, N.Y.)*, 325(5939):487–90.

- [48] Riffell, J. a. and Zimmer, R. K. (2007). Sex and flow: the consequences of fluid shear for sperm-egg interactions. *The Journal of experimental biology*, 210(Pt 20):3644–3660.
- [49] Rinker, R. G. (1979). Transport in porous catalyts. *AIChE Journal*, 25(1):205–206.
- [50] Rusconi, R., Guasto, J. S., and Stocker, R. (2014). Bacterial transport suppressed by fluid shear. *Nature Physics*, 10(3):212–217.
- [51] Rutllant, J., López-Béjar, M., and López-Gatius, F. (2005). Ultrastructural and rheological properties of bovine vaginal fluid and its relation to sperm motility and fertilization: A review.
- [52] Ryan, J. N. and Elimelech, M. (1996). Colloid mobilization and transport in groundwater. *A: Physicochemical and Engineering Aspects*, 107:1–56.
- [53] Schnaar, G. and Brusseau, M. L. (2006). Characterizing Pore-Scale Dissolution of Organic Immiscible Liquid in Natural Porous Media Using Synchrotron X-ray Microtomography. *Environmental Science & Technology*, 40(21):6622–6629.
- [54] Sipos, O., Nagy, K., Di Leonardo, R., and Galajda, P. (2015). Hydrodynamic Trapping of Swimming Bacteria by Convex Walls. *Physical Review Letters*, 114(25):1–5.
- [55] Taktikos, J., Stark, H., and Zaburdaev, V. (2013). How the motility pattern of bacteria affects their dispersal and chemotaxis. *PLoS ONE*, 8(12).
- [56] Unice, K. M. and Logan, B. E. (2000). Insignificant Role of Hydrodynamic Dispersion on Bacterial Transport. *Journal of Environmental Engineering*.
- [57] Uppaluri, S., Heddergott, N., Stellamanns, E., Herminghaus, S., Zöttl, A., Stark, H., Engstler, M., and Pfohl, T. (2012). Flow loading induces oscillatory trajectories in a bloodstream parasite. *Biophysical Journal*, 103(6):1162–1169.
- [58] Velraeds, M. M. C., Van De Belt-Grltter, B., Van Der Mei, H. C., Reid, G., and Busscher, H. J. (1998). Interference in initial adhesion of uropathogenic bacteria and yeasts to silicone rubber by a Lacto bacillus acidop hilus b i osu rf a c t a n t. *J. Med. Microbiol*, 47:1081–1085.
- [59] Weiss, T., Mills, a., Hornberger, G., and Herman, J. (1995). Effect of bacterial cell shape on transport of bacteria in porous media. *Environmental Science & Technology*, 29(7):1737–1740.
- [60] Whitesides, G. M. (2006). The origins and the future of microfluidics. *Nature*, 442(7101):368–73.
- [61] Xia, Y. N. and Whitesides, G. M. (1998). Soft Lithography. *Annual Review of Materials Science*, 37(5):551–575.
- [62] Yadroitsev, I., Shishkovsky, I., Bertrand, P., and Smurov, I. (2009). Manufacturing of fine-structured 3D porous filter elements by selective laser melting. *Applied Surface Science*, 255(10):5523–5527.

Appendix A

Determination of Flow Fields within Microfluidic Porous Media

A.1 Particle Tracking Velocimetry Flow Field Measurements

In order to obtain the flow fields in the microfluidic channel experimentally, suspensions of fluorescent $0.5 \mu\text{m}$ particles were flowed at a flow rate of $2 \mu\text{L}/\text{min}$ in the channels with different lattice angles. The tracer particles were tracked from the videos recorded via fluorescence microscopy using the same microscope and camera as in the bacterial flow experiments. Flow field measurements were performed in approximately the same location within the microfluidic porous medium as the bacterial experiments. Similar to the method explained in section 2.3.1, the relative positions of the particles were obtained in each unit cell. The unit cell was binned to a 120×120 square grid and the velocity at each bin was obtained by interpolating the instantaneous velocities of the particles. The flow fields in Fig. 2.1 C were obtained using this method.

A.2 Numerical Simulations of Flow Fields

Due to optical limitations, the measured flow fields were not fully resolved in locations close to the pillars. As explained in 2.2.3, we used finite element analysis (Comsol Multiphysics) to determine

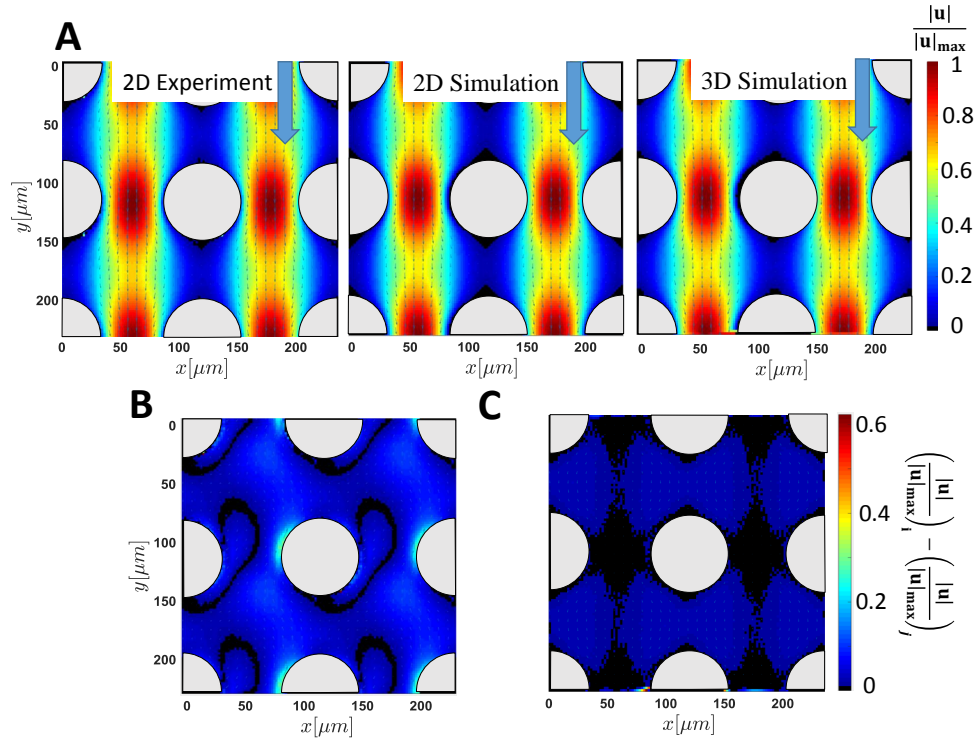


Fig. A.1 Comparison of flow fields obtained from tracer particle tracking and numerical simulations in 2D and 3D. **A**, Flow fields in $\theta = 0^\circ$ lattice obtained from tracking $0.5 \mu\text{m}$ fluorescent particles and solving Stokes flow equations in a 2D and 3D geometry normalized by the maximum magnitude of velocity. **B**, Absolute difference between flow fields in **A** obtained from experiments and 2D simulations. **C**, Absolute difference between flow fields in **A** obtained from 2D and 3D simulations.

the flow fields in the middle depth of our model porous medium with a higher resolution around the pillars. We assumed that the dominant flow gradients are in the imaging plane of the porous microchannel, so a 2D geometry was used to obtain flow fields for different angles. In order to verify the robustness our assumption, we also solved Stokes equations for a 3D geometry of the model porous medium with $\theta = 30^\circ$ lattice and a depth identical to the actual microfluidic channel. The length and width of the channel and the number of pillars were identical to the 2D geometry. Figure A.1 shows the flow fields of the $\theta = 0^\circ$ lattice normalized by the maximum magnitude of the velocity, and Fig. A.1 verifies that the absolute difference of these normalized flow fields is sufficiently small. Thus, 2D simulations were used to efficiently obtain flow fields and their gradients throughout the work presented here.

Appendix B

Dead Cell Experiments

In order to understand the effect of the finite sizes of the bacteria on their distributions in the model porous media, suspensions of dead cells were flowed at $2 \mu\text{L}/\text{min}$ in the microfluidic porous channel with $\theta = 0^\circ$. The bacteria were fixed in a 2% formaldehyde solution that is reported to preserve the morphology of the cells [14]. Imaging and tracking was performed as previously described in the swimming cell experiments to obtain the dead cell number density map (Fig. B.1 A). The finite size of the dead cells excludes them from the streamlines passing nearest to the pillars and subsequently through low velocity regions, resulting in zero cell density between pillars in the stream-wise direction. The effective diameter of the cells were estimated by comparing their density distributions with the particle density maps of suspensions of microspheres with diameters of $5 \mu\text{m}$ and $10 \mu\text{m}$ flowing in the same porous channel at $2 \mu\text{L}/\text{min}$ (Fig. B.1 B and C respectively). Since the width of the low density exclusion region falls between the density maps in Fig. B.1 B and C, the effective diameter of the bacteria was chosen to be the average of the diameter of the particles, $7.5 \mu\text{m}$, for the Langevin simulations. This effective size is consistent with the size of the *B. subtilis* cells. We further note that the asymmetry in the density distributions results from the minor misalignments of the pillars from the microfabrication process. This imperfection causes asymmetries in the flow fields and affects the motion of particles as they are advected downstream.

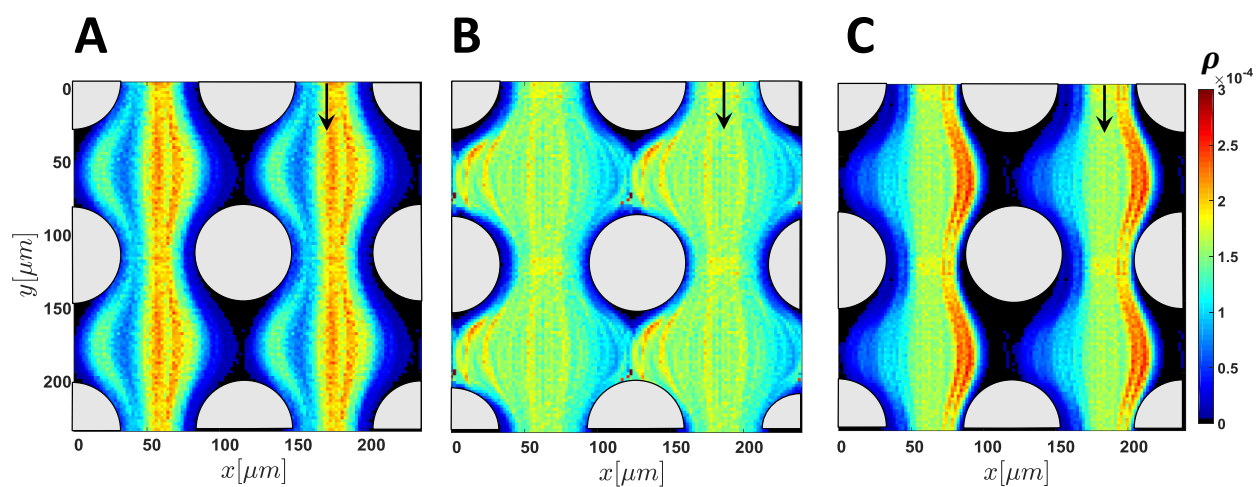


Fig. B.1 Particle number density maps for dead cells and microspheres in $\theta = 0^\circ$ lattice. **A**, Dead Cells, **B**, 5 μm diameter spheres, and **C**, 10 μm diameter spheres

Appendix C

Ratcheting Effects in the $\theta = 7.5^\circ$ Lattice

The center of the Gaussian profile of the probability density functions for the transverse cell displacements in the porous pillar lattice with $\theta = 7.5^\circ$ exhibits a shift to the right in presence of flow. This drift is due to the well-known ‘ratcheting’ of finite sized particles including bacteria (C.1 A and B). Ratcheting occurs due to the steric repulsion of bacteria from the solid pillars that prevents the bacteria from following a set of streamlines that pass nearest to the pillars (similar to the exclusion zones in Appendix B). For a regular lattice oriented at an angle relative to the mean flow, the bacteria are pushed slightly to the right each time then encounter a subsequent pillar resulting in a net drift. This mechanism has been widely exploited for separating particles with different sizes [5] (Fig.C.1 C). Ratcheting was only observed in our experiments for $\theta = 7.5^\circ$. Since ratcheting causes non-diffusive behavior in the mean squared displacement curves, the effective diffusion coefficients of the bacteria in Fig. 4.3 were calculated by fitting the probability distributions of the transverse displacements of the bacteria with the Gaussian profile of diffusion in 1D using:

$$p(\Delta x, \Delta t) = \frac{1}{(4\pi D_{\perp} \Delta t)^{1/2}} e^{-\frac{(\Delta x - \mu)^2}{4D_{\perp} \Delta t}}. \quad (\text{C.1})$$

where D_{\perp} is the effective diffusion of bacteria, and μ is the center of the Gaussian profile. To ensure that the fitting is performed after the profiles become Gaussian, we considered 10 profiles to be fitted at times $\Delta t = 20 - 30$ s that are long compared to the persistence time of the swimming

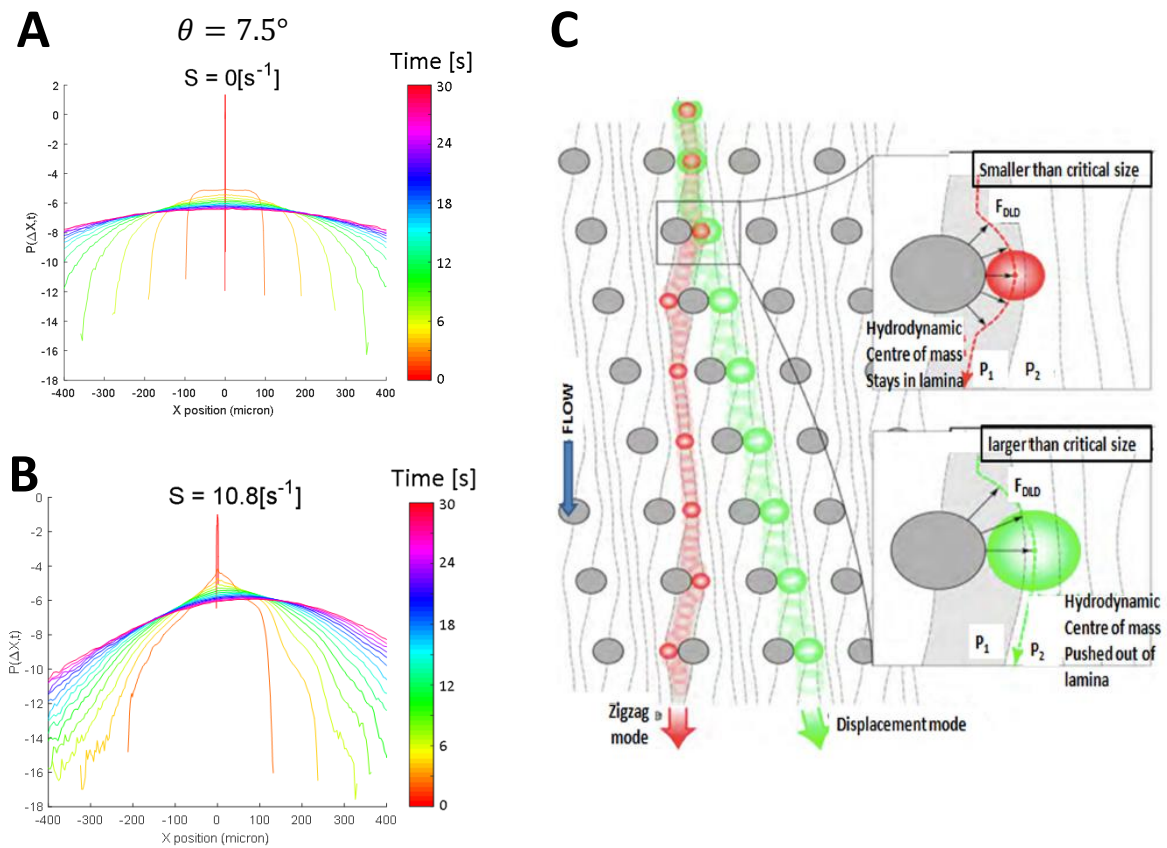


Fig. C.1 **Ratcheting in a porous lattice with $\theta = 7.5^\circ$** **A - B**, Probability distributions of displacements of the bacteria in the transverse direction of the flow in the $\theta = 7.5^\circ$ lattice obtained from simulations in a quiescent fluid (**A**) and in the presence of flow (**B**). **C**, The ratcheting effect is well known and has been used extensively for sorting particles based on their sizes [5]

bacteria ($\tau_p = 1$ s). The diffusion coefficients obtained from those fits were averaged to obtain the effective diffusion coefficient of bacteria for each mean shear rate.

Appendix D

Effect of Porosity on Bacterial Densification and Transport

In groundwater and hydrology studies, the typical porosities of porous materials (e.g. sand) fall between 0.3 - 0.45 [1, 53]. While the shear rates in these systems are typically in the range of our model experiments, the average flow speeds are significantly lower due to the smaller pore sizes. To examine the effect of porosity, we increased the pillar diameter in the $\theta = 0^\circ$ lattice simulations to 100 μm to have a porous medium with a porosity of 0.45. We performed Langevin simulations in this lattice with mean shear rates 0, 4, and 10 s^{-1} , with all other parameters held constant. Heterogeneous bacterial distributions are still observed with increasing shear rate (Figure D.1 A). However, the steric exclusion effects become stronger due to the narrow throats between pillars. Bacteria are thus prevented from reaching the low velocity regions between the pores in the stream-wise direction because of their finite size. Analysis of the transport of the bacteria in the transverse direction of the mean flow direction shows that the probability distribution of displacements becomes narrower in the presence of shear and there are offsets between the mean squared displacement profiles after they become diffusive. These results again indicate reduced effective diffusivity of the bacteria by increasing shear (Fig. D.1 B-D), however the effects are not as severe as in the high porosity case explored in the body of the thesis.

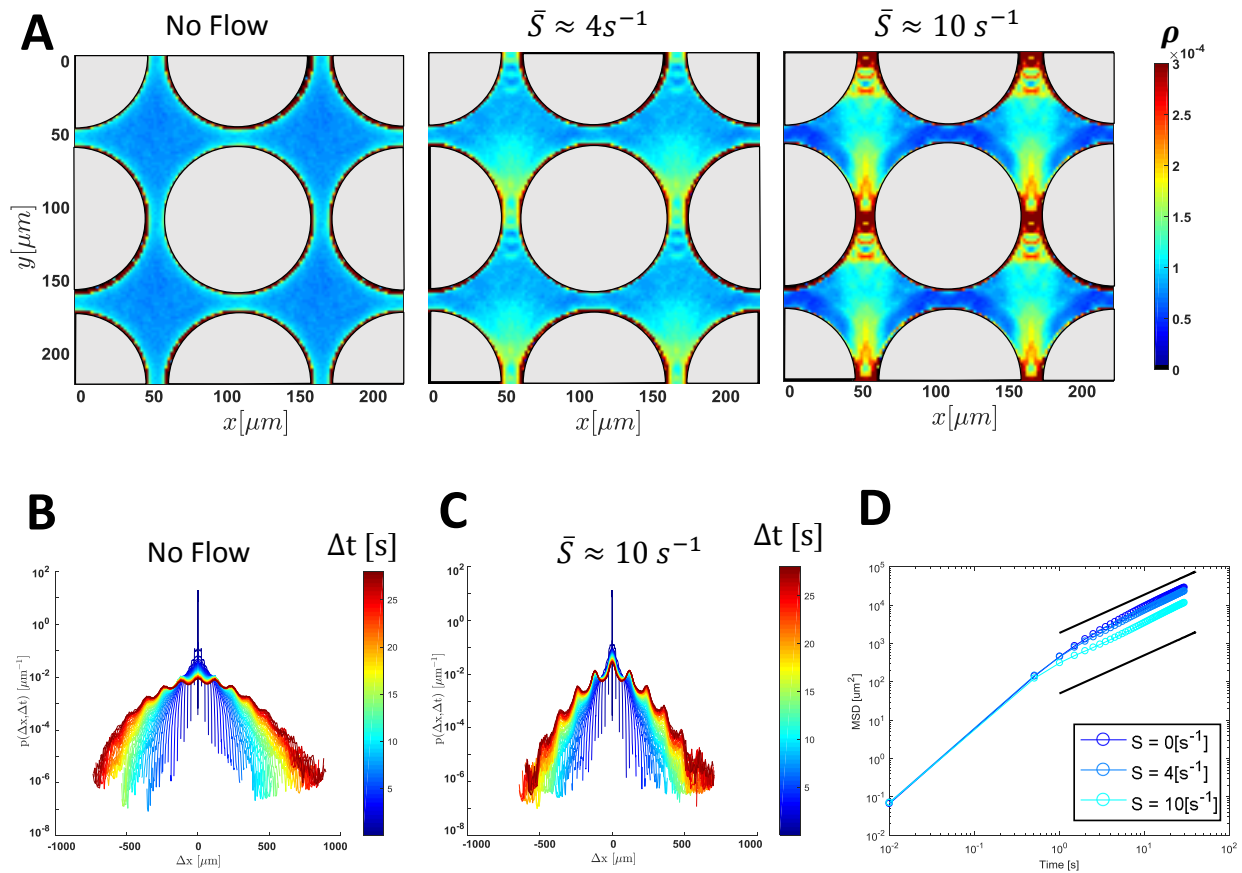


Fig. D.1 Shear trapping at low porosity: Langevin simulations in $\theta = 0^\circ$ lattice with 0.45 porosity. **A**, Bacteria number density maps in mean shear rates $\bar{S} = 0, 4,$ and 10 s^{-1} . **B**, Probability distribution of displacements in the absence of flow. **C**, Probability distribution of displacements for $\bar{S} = 10 \text{ s}^{-1}$ in the transverse direction of the mean flow direction. **D**, Mean squared displacements of bacteria in mean shear rates $\bar{S} = 0, 4,$ and 10 s^{-1} in the transverse direction of the flow.